

A ^{13}CO and C^{18}O Survey of the Molecular Gas Around Young Stellar Clusters Within 1 kpc of the Sun

Naomi A. Ridge

Five College Radio Astronomy Observatory, Dept. of Astronomy, University of Massachusetts, Amherst, MA 01003, USA

naomi@fcrao.umass.edu

T.L. Wilson

Submillimeter Telescope Observatory, University of Arizona, Tucson, AZ 85721, USA & Max Planck Institut für Radioastronomie, Auf dem Hügel 69, 53121 Bonn, Germany

S.T. Megeath, L.E. Allen & P.C. Myers

Harvard-Smithsonian Center for Astrophysics, 60 Garden Street, Cambridge, MA 02138, USA

ABSTRACT

As the first step of a multi-wavelength investigation into the relationship between young stellar clusters and their environment we present fully-sampled maps in the J=1–0 lines of ^{13}CO and C^{18}O and the J=2–1 line of C^{18}O for a selected group of thirty young stellar groups and clusters within 1 kpc of the Sun. This is the first systematic survey of these regions to date. The clusters range in size from several stars to a few hundred stars. Thirty fields ranging in size from $8' \times 8'$ to $30' \times 60'$ were mapped with $47''$ resolution simultaneously in the two J=1–0 lines at the Five College Radio Astronomy Observatory. Seventeen sources were mapped over fields ranging in size from $3' \times 3'$ to $13' \times 13'$ in the J=2–1 line with $35''$ resolution at the Submillimeter Telescope Observatory. We compare the cloud properties derived from each of the three tracers in order to better understand systematic uncertainties in determining masses and linewidths. Cloud masses are determined independently using the ^{13}CO and C^{18}O transitions; these masses range from 30 to 4000 M_{\odot} . Finally, we present a simple morphological classification scheme which may serve as a rough indicator of cloud evolution.

Subject headings: circumstellar matter — ISM: clouds — radio lines: ISM — stars: formation

1. Introduction

It is well established that most stars form in clusters. For example, in an analysis of the 2MASS second incremental release catalogue of the Orion A, Orion B, Perseus and Monoceros molecular clouds, Carpenter (2000) found a total of 1200 isolated stars and ~ 3000 stars in fourteen clusters, six of these clusters with more than 100 members each. Hodapp (1994) performed a K' -band survey of 165 regions with known molecular outflows, and found that one third of the outflows were located within a cluster of stars. Clustered star formation spans an enormous range in the number of stars from small groups of several stars in the Taurus dark clouds to the largest known young cluster in our galaxy, NGC 3603, containing many thousands of stars and finally to proto-globular clusters containing up to one million stars. A complete understanding of star formation therefore requires a theory which describes the full range of star formation from small groups to globular clusters.

The formation of stars in clusters is thought to occur over a ~ 1 Myr time span (e.g. Hillenbrand 1997; Palla & Stahler 2000), during which the material to form stars is continually drawn from a reservoir of molecular gas. It is from this reservoir, through a process not fully understood, that fragments condense out of the gas and collapse to form stars. It is therefore likely that the rate of star formation and the number of stars which ultimately form depend on the properties of the molecular reservoir. Previous studies have observed a clear difference between the molecular gas in regions containing small groups of stars, such as Taurus, and regions containing large clusters, such as Orion (Jijina et al. 1999; Onishi et al. 1996; Lada et al. 1991; Lada 1992; Carpenter et al. 1990, 1995; Tieftrunk et al. 1998). A systematic study of the molecular gas in clusters spanning a range in the number and density of constituent stars can probe in detail how the properties of the parental cluster-forming gas dictates the properties of the forming clusters.

Such a systematic survey could also provide a better picture of the evolution of the cluster-forming molecular gas. The young stars are thought to dissipate the parental cluster-forming gas through winds and radiation, resulting in the termination of ongoing star formation; however, the timescale and exact mechanism of the dissipation remains poorly understood. The process of gas dissipation has been studied in the vicinity of Herbig Ae/Be stars by Fuente et al. (1998a, 2002, hereafter FMBRP), most of which are members of clusters. While these observations provide insight into the mechanism and timescale for the dissipation of gas around individual stars, the dissipation of the extended cluster-forming gas remains to be studied in detail.

We have therefore begun a program of multi-wavelength observations which, when combined with existing infrared and optical data, will yield detailed information about both the stars and their surrounding gas in a large sample of young stellar groups and clusters within

1 kpc of the sun. The final data set will include sensitive ground based wide-field optical and near-infrared imaging and spectroscopy, millimeter spectral-line and continuum maps and mid-infrared observations obtained with the Space Infrared Telescope Facility (SIRTF). Once complete, it will be made available to the community via a web-based database, providing an invaluable resource for future star-formation studies.

In this paper we present our ^{13}CO and C^{18}O molecular line data. C^{18}O is an excellent tracer of the column density in the warm, dense gas typical of cluster forming regions (Goldsmith, Bergin, & Lis 1997). Although the freeze out of C^{18}O has been observed in cold, dark clouds (Bergin et al. 2002), this should only affect small pockets of cold, dense gas within each cluster, such as gravitationally unstable fragments of gas undergoing collapse. The overall structure of the warm gas pervading the cluster is expected to be well traced by C^{18}O . In addition to tracing the structure of the molecular gas, the C^{18}O lineshapes and velocities are good tracers of the gas kinematics and are relatively unaffected by optical depth effects. Although emission from the more abundant ^{13}CO can be optically thick toward the cluster center, the ^{13}CO emission can be traced further into the outer, more tenuous regions of the cluster where C^{18}O is too weak to be mapped efficiently. These data therefore enable us to characterise the cluster-forming molecular gas from the regions of peak density toward the centers of each cluster out to the non-star-forming gas of the surrounding molecular cloud. Here we concentrate on examining general trends in the morphological properties of the cluster gas. Detailed analysis of the gas kinematics in each of the individual sources will be presented in subsequent papers (Ridge et al. in prep.).

Section 2 describes how our sources were selected, section 3 gives details of the observing and data reduction procedures. An “atlas” of the clusters is presented and cluster properties are compared in section 4. Finally we summarise our main conclusions in section 5.

2. The Sample

To provide a rich sample of sources which are relatively nearby and thus can be observed with high angular resolution and sensitivity, we have compiled from the literature a list of all known young stellar clusters within 1 kpc of the Sun (Christopher et al. in prep.). This list contains a remarkable diversity of regions from small groups with several stars to dense clusters containing hundreds of stars. We use the term “cluster” in this paper to refer to both small groups with five or more stars, and large clusters of several hundred stars. Only these large clusters may eventually form bound open clusters after the dissipation of their parental molecular gas, while most of the smaller systems should quickly disperse (Adams & Myers 2001). Here we present the subset of regions that are easily observable from the north.

Clusters in the regions of Orion and Ophiuchus are not included as they are well studied in the literature. A full list of the objects in the survey, their distances, and the co-ordinates we adopted as the map center for each is given in table 1. Where available in the literature the number of stars in the cluster is also given, and a brief summary of previous observations of each source is included in appendix A.

The IRAS point source catalogue was searched for objects within $3'$ of each of the map centers. Where no source could be located within this radius, the search radius was increased in $30''$ increments until at least one IRAS point source was found. Far-infrared (FIR) luminosities were calculated from the 12– $100\mu\text{m}$ IRAS fluxes using the following formula (Casoli et al. 1986):

$$\frac{L_{\text{FIR}}}{L_{\odot}} = 4.7 \times 10^{-6} D^2 \left(\frac{S_{12}}{0.79} + \frac{S_{25}}{2} + \frac{S_{60}}{3.9} + \frac{S_{100}}{9.9} \right), \quad (1)$$

where D is the distance in pc and S_{λ} is the flux density in Jy. These luminosities are also listed in table 1. If more than one IRAS source was found within the search area then the luminosity of the brightest source is listed. We will use the FIR luminosity in this paper as an indicator of the size (mass) of the stellar component of the clusters, but for more evolved clusters, such as IC 348, where most of the stars are optically visible this assumption is not valid.

Figure 1a shows a histogram of the number of sources with distance. The solid line represents the full sample and the dashed line indicates those sources which were observed at both the Five College Radio Astronomy Observatory (FCRAO) and the Submillimeter Telescope Observatory (SMTO). The histograms show the wide range of distances toward our sample regions, which spans a factor of seven from the nearby L 1551 dark cloud to the distant GGD 4 cluster. This translates into a factor of seven in spatial resolution. The biases this may introduce in a comparative analysis of the clusters are mitigated by the range of cluster properties sampled at a given distance, as shown in Figure 1b. Although there is a trend of increasing FIR luminosity with distance, the upper and lower envelope of this trend differ by a factor of one hundred in luminosity. Furthermore, biases due to distance can be eliminated by comparing regions in the same molecular cloud. In particular, we have two or more clusters within the Perseus cloud, NGC 1499 cloud, Monoceros cloud, the Cepheus cloud, and the Cepheus Bubble. By studying clusters within a single cloud or cloud complex, we can undertake comparative studies which are unaffected by variations in spatial resolution, spatial coverage, or sensitivity.

3. Observations and Data Reduction

3.1. FCRAO Observations

Observations in the ^{13}CO 1–0 (110.201 GHz) and C^{18}O 1–0 (109.782 GHz) transitions were carried out during several periods between 2001 December and 2002 November at the FCRAO 14m telescope in New Salem, Massachusetts, mostly during the commissioning stage of the On-the-Fly (OTF) mapping technique. OTF maps of each of the clusters were made using the SEQUOIA 16-element focal plane array and a dual-IF narrow-band digital correlator, enabling maps in ^{13}CO and C^{18}O to be obtained simultaneously. Observations made after 2002 March utilised the upgraded SEQUOIA-2 array with 32 elements. The correlator was used in a mode which provided a total bandwidth of 25 MHz, with 1024 channels yielding an effective velocity resolution of 0.07 km s^{-1} . For a few objects (see table 2) data was obtained in the 50 MHz bandwidth mode, with a velocity resolution of 0.13 km s^{-1} . The weather was exceptionally stable during the runs with system temperatures at 110 GHz generally between 200 and 400 K (single sideband).

Maps were obtained by scanning in the RA direction, and an “off” source reference scan, was obtained after every two rows. Off-positions were checked to be free of emission by performing a single position-switched observation with an additional 30' offset. Map sizes are given in table 2. A data-transfer rate (DTR) of either 1 or 2 Hz was used, and in some cases the full size maps were built up from several smaller submaps. When a DTR of 2 Hz was used, maps were repeated to increase signal-to-noise. Calibration was by the chopper wheel technique (Kutner & Ulich 1981), yielding spectra with units of T_{A}^* . Pointing was checked regularly and found to vary by less than $5''$ rms.

The OTF technique was implemented at FCRAO in order to compensate for the removal of the dewar rotation system in the summer of 2001. The maps obtained are therefore not evenly sampled and a convolution and regridding algorithm has to be applied to the data in order to obtain spectra on a regularly sampled grid. This process was carried out using software provided by the observatory (Heyer, Narayanan, & Brewer 2001). Using this software the individual spectra have a linear baseline subtracted, then are convolved onto a regular $25''$ grid weighted by $1/\text{rms}^2$, yielding a Nyquist sampled map, and corrected for the main beam efficiency of the telescope, which is 0.48 at 110 GHz.

After regridding, the individual spectra had an rms sensitivity of $\sim 0.2 \text{ K}$ per 25 kHz channel (see table 2), with the OTF technique yielding maps with extremely uniform sensitivity. Additionally, the simultaneous observation of the two lines gives perfect registration between the ^{13}CO and C^{18}O maps.

3.2. SMTO Observations

Observations in the $C^{18}O$ 2–1 (219.560 GHz) transition were carried out at the Heinrich-Hertz Telescope (HHT) during several periods in the winter and spring of 2001–2002. The receiver was a single channel SIS mixer with a double sideband receiver noise temperature of about 120 K, depending on receiver tuning. The total (single sideband) system noise temperature was between 270 and 500 K depending on weather. The telescope beamsize was $35''$ at the line frequency. The pointing was checked on well known calibrators or planets, and found to be $2''$ rms. The main beam efficiency was measured to be 0.78 at the line frequency. However, because of 30% variations in the sideband ratios, the results were scaled to measurements of standard regions such as the Orion KL nebula. Spectra have units of T_A^* .

The data were taken employing OTF mapping. The procedure was first to perform a hot-sky calibration using a chopper wheel, then to map a $2'$ by $2'$ or $2.5'$ by $2.5'$ region. These regions were mapped by scanning in R.A. with a $15''$ separation between the Declination rows. A reference region either $10'$ or $15'$ lower in R.A. and offset from the center of the map, was used. A measurement on the reference position, which had been previously checked for the presence of emission, was taken before measuring each row. The raw OTF maps were convolved with a Gaussian beam and regridded onto a regular $15''$ grid in the *GILDAS* data reduction environment. The final images consist of mosaics of the individual OTF maps. After the regridding process, individual spectra had an rms sensitivity of $\lesssim 0.17$ K per 250 kHz ($=0.34$ km s $^{-1}$) channel.

4. Results

Integrated intensity maps of the ^{13}CO 1–0 and $C^{18}O$ 1–0 emission are presented in figures 2 through 13. The ^{13}CO 1–0 maps have contours at 10% to 100% of the maximum integrated intensity with intervals of 10%, except where indicated otherwise in the caption. The base contour level is $\gg 3\sigma$. The $C^{18}O$ 1–0 maps have a base contour level of 3σ , with contours at 1σ intervals in most cases. In a few sources different contour levels are used, and are described in the captions. Integrated intensity maps of the $C^{18}O$ 2–1 emission are presented in figures 14 through 17, with contours at 10% to 100% of the maximum integrated intensity. The value of the maximum integrated intensity in each map is given in the top right corner of the figures for reference. We have indicated the positions of known stellar or protostellar sources in the regions by triangles (embedded sources) or stars (optically-visible sources). The $C^{18}O$ 1–0 emission was too weak to be detected in only two sources, HD 216629 and VV Ser. This was particularly surprising in HD 216629 where the ^{13}CO emission was

relatively strong at the peak position.

4.1. Morphology

The clusters show a range of morphologies, from compact, roughly spherical (e.g. CB34), cometary (e.g. S140) to diffuse, extended emission (e.g. VVSer). Based on our examination of the ^{13}CO and C^{18}O maps, we have assigned each source a morphological description, which is listed in table 3. Some of the sources could be placed in more than one category, for instance NGC 7129 shows both a compact core and a cavity. Many of the sources show cores surrounded by more extended envelopes. The emission rarely exhibits circular symmetry; the cores are usually somewhat elongated, and their envelopes are often more elongated than the cores, possibly because the larger envelopes are better resolved. In some cases an elongated core in ^{13}CO appears as a chain of multiple cores when observed in C^{18}O which is less affected by optical depth (e.g. IC 348). In many cases, multiple peaks are apparent; we have tabulated the number of “significant peaks” (N_{peaks}) detected in ^{13}CO for each region in table 3. We have used the ^{13}CO data to identify peaks due to the higher signal to noise in this tracer; however, in several cases, additional peaks are apparent in the C^{18}O maps due to the lower optical depth in the C^{18}O lines.

In many of the clusters, the most luminous members have been identified, either through the IRAS point source catalog, or through catalogs of Herbig Ae/Be stars (Testi et al. 1997, 1998). As an indicator of whether the observed ^{13}CO peaks contain known sites of recent or ongoing star formation, the distance (d_*) between the embedded source or star and its nearest ^{13}CO peak is shown for each source in table 3. In cases where there are multiple peaks and/or stars, the smallest distance is reported.

The observed structures in the ^{13}CO and C^{18}O maps are most likely a combination of features due to initial conditions in the cloud and interaction with already formed stars. The compact cores, such as GGD 4 and CB34 are likely to be still close to their initial state, while clouds with cavities such as HD 200775 are breaking apart due to star-cloud interactions. Most of the Herbig Ae/Be type stars in the sample appear to be located in regions which have morphologies consistent with dispersal of their surrounding molecular gas, while the embedded sources appear to be preferentially located in gas which is more centrally condensed. Nineteen of the thirty regions have ^{13}CO peaks coincident with or close to a stellar or IRAS position. All but two of these display a centrally condensed morphology (core or core + envelope). We therefore interpret the proximity of the stellar source to the map peak as an indicator of youth of the region. Based on these interpretations we propose a sequence of morphologies, or “developmental classes” as follows:

- I** A single significant peak in ^{13}CO and C^{18}O indicative of one dominant molecular core. An extended envelope is commonly detected around the core. An embedded source is found within the 50% contour of the peak C^{18}O emission, e.g. CB34. Eleven of the clusters fall into this class, including a subset of five bright-rimmed globules, noted by “BRG” in table 3. The BRGs all show “tails” of extended ^{13}CO emission.
- II** The ^{13}CO and C^{18}O emission is distributed in multiple peaks and/or elongated filaments, often with an extended envelope. An embedded source falls within the 50% contour of a C^{18}O peak or filament, e.g. S171. In some cases with two known associated sources (e.g. NGC 7129), one of the sources is located outside of peaks. Ten sources fall into this class.
- III** Known stars fall well outside of ^{13}CO and C^{18}O peaks and filaments, e.g. HD 200775. Typically show diffuse, extended emission, multiple ^{13}CO peaks, and multiple or no C^{18}O peaks. In one region, IC348, two of the three associated sources fall outside the ^{13}CO emission. Nine sources fall into Class III.

The classifications are listed in table 3, and figures 2 through 10 are grouped according to classification. Since many of the Class I and III sources show similar FIR luminosities, it is likely that the differing morphologies reflect an evolutionary progression from Class I to Class III driven by the disruption of the gas by the embedded stars. Due to their morphological complexity, Class II sources are more problematic. Many of these regions may be coeval with Class I sources, indicating different initial conditions, while others showing distinct signs of gas dispersion (e.g. NGC 7129) may be in an intermediate evolutionary state between Class I and III.

This scheme differs from the the classification scheme of Fuente et al. (1998a, 2002), although the Fuente et al. sample contains several sources in common with this work. Fuente et al. mapped small regions (~ 1 pc) around each of their sources in order to determine the molecular gas distribution close to the Herbig Ae/Be stars, while in contrast, our proposed classification is based on the global morphology of the cluster forming cloud. However, of the six sources common to both Fuente et al. and this work (MWC 297, HD 200775, HD 216629, VV Ser, BD+65°1637 and LkH α 234¹), both classification schemes place these sources as the most evolved regions of the sample, with one exception, NGC 7129, but this is due to our treatment of the region as a whole, while Fuente et al. considered the two stellar sources separately. We see significant molecular gas emission away from the location of the star, and outside the region covered by Fuente et al. in most cases.

¹Both these last two fall within the region of NGC 7129 we observed

4.2. Masses

The core masses determined from the three isotopomers/transitions are given in table 4. Gas masses were determined from the ^{13}CO and C^{18}O 1–0 transitions using a local thermal equilibrium (LTE) approximation, assuming an excitation temperature of 20 K and the distances given in table 1. This method has been found to be accurate to within a factor of 2–4 (Rohlfs & Wilson 2000) as long as the actual excitation temperature is less than 30 K. Such high excitation temperatures are expected only toward the embedded OB stars that occupy a small fraction of the total cloud area in any of these regions. The C^{18}O 2–1 masses were determined by calculating the column density of H_2 from the large velocity gradient (LVG) relation:

$$N_{\text{H}_2} = 2.65 \times 10^{21} \int T_{\text{MB}}(\text{C}^{18}\text{O}, J = 2 \rightarrow 1) dv, \quad (2)$$

where v has units of km s^{-1} , T_{MB} of Kelvins and N_{H_2} is given in cm^{-2} (Rohlfs & Wilson 2000). N_{H_2} can then be converted to a total gas mass by assuming a distance (as given in table 1), the mass of the hydrogen molecule and a helium abundance. For comparison, we have also calculated the LTE mass from the C^{18}O 1–0 emission for the smaller area covered by the C^{18}O 2–1 observations (hereafter referred to as the central C^{18}O mass) and this is given in column 5 of table 4.

We compare the masses derived from each of the three transitions in figure 18, in order to investigate how the choice of tracer and map size will affect our results. Figure 18b shows the central C^{18}O 2–1 mass plotted against the central C^{18}O 1–0 mass. The central mass determinations for the two C^{18}O transitions are very consistent, indicated by the dashed line showing the 1:1 relation. Just two sources, GGD 12-15 and CepC fall significantly from this relation. This plot demonstrates that mass estimates from different transitions using different approximations (LTE vs LVG) lead to equivalent results. Comparison of the central C^{18}O 2–1 masses, measured with the SMTO, and the total C^{18}O 1–0 masses in the larger region covered by the FCRAO observations (fig.18c) indicates that a significant fraction of the gas ($\sim 65\%$) is found in emission that extends outside the smaller C^{18}O 2–1 maps. Nevertheless, a clear correlation is evident, suggesting that the mass in the extended component grows linearly with the mass in the central region.

The correlation between the envelope mass and the central mass is also apparent in the strong correlation ($\sim 9\sigma$) between the ^{13}CO and C^{18}O 1–0 masses (Figure 18a). However, the ^{13}CO masses are approximately a factor of two larger than the masses determined from the C^{18}O 1–0 emission. This is indicated by the solid line on figure 18a which is a least-squares-fit (LSF) to the data, with a slope of 0.58 ± 0.05 . The ^{13}CO traces lower density gas since the abundance is 5 to 10 times higher than C^{18}O and also because photon trapping

allows the ^{13}CO to be excited at a lower density than C^{18}O . In addition, the $J=1-0$ line is more easily excited than the $J=2-1$ line because the Einstein A coefficient is about a factor of 8 smaller. Therefore the ^{13}CO emission is detectable in more extended regions, where the C^{18}O emission is too weak to detect, and is likely to be mostly due to gas in the envelope which is too diffuse to detect in the weaker C^{18}O line. The relationship between the 'central' (C^{18}O 2–1) and 'total' (^{13}CO 1–0) masses shows a strong correlation ($\sim 9\sigma$) with small scatter (Figure 18d). This is surprising considering the varied morphologies of the sources and the fact that the physical size of the region mapped varies with distance. The line represents a LSF with a slope of 0.23 ± 0.02 , indicating that the central mass is usually $\sim 1/4$ of the total mass.

Histograms of the ^{13}CO 1–0 masses are presented in figure 19. These show that 2/3 of the clouds are below $1000 M_{\odot}$ when measured with ^{13}CO , and that 1/3 of the clouds are below $500 M_{\odot}$. Figure 20a shows the C^{18}O 1–0 masses as a function of distance. Although there is an apparent trend of higher mass with distance, the upper and lower envelope of this trend differ by more than an order of magnitude. This wide range of masses present at any distance interval will minimise biases due to distance in subsequent comparisons of cloud vs. cluster properties. Finally, the C^{18}O 1–0 mass is plotted against the FIR luminosity in figure 20b. The correlation here ($\sim 4\sigma$), indicating that more massive cores are forming more luminous (massive) stars, is much stronger than any correlation between either mass or FIR luminosity and distance (both $\lesssim 2\sigma$) and therefore this effect is likely to be real.

4.3. Sizes and Linewidths

The sizes and linewidths of the cores are listed in Table 5. We define core size, R , here as $\sqrt{A/\pi}$ where A is the total area in pc^2 (i.e. number of pixels \times pixel size in pc) where the integrated intensity is $\geq 1/2$ the maximum integrated intensity. All the derived sizes are much larger than the telescope resolution, and smaller than the map size. The average FWHM linewidth in the cores was determined by combining all the spectra in the regions of the maps where emission was detected, and then fitting a Gaussian profile to the resultant average spectrum. In a few cases (e.g. Mon R2, S 140 and Ceph A) this is likely to be affected by strong outflows. Note that for multiply-peaked or filamentary sources the definitions of size we make here may not be appropriate; this definition is most applicable to sources which show some degree of circular symmetry.

We compare the linewidths of the 1–0 and 2–1 transitions in figure 21. The C^{18}O 2–1 linewidth is closely correlated with the C^{18}O 1–0 linewidth with a best-fit slope close to one. This is expected given the low optical depth of the C^{18}O transitions. When the two

linewidths do differ, the linewidth given by 2–1 transition is in all but two cases smaller. This is likely an effect of the larger field covered with C¹⁸O 1–0 – the inclusion of a larger region of the cloud should typically broaden the average linewidth due to velocity shifts across each map. In most cases, however, the average linewidths are dominated by the stronger line emission in the centers of each region, resulting in the strong correlation seen in figure 21a. The ¹³CO and C¹⁸O 1–0 linewidths do not show the same degree of correlation (figure 21b), with the ¹³CO linewidths typically being higher. This likely due in part to the higher optical depth in the ¹³CO line.

We also calculate the virial mass, M_V , from the tabulated sizes and linewidths using the form of the virial theorem given in Rohlfs & Wilson (2000):

$$\frac{M_V}{M_\odot} = 250 \left(\frac{\Delta v_{1/2}}{km\ s^{-1}} \right)^2 \left(\frac{R}{pc} \right). \quad (3)$$

The gas mass derived from the C¹⁸O 1–0 data using the LTE analysis and virial theorem are compared in figure 22. The majority of sources show virial masses between one to two times larger than the C¹⁸O mass. This difference will be reduced by the choice of the virial constant; for clouds with r^{-2} density profiles, the virial masses we have calculated will be a factor of two too large (MacLaren et al. 1988). Furthermore, the virial theorem should only be applicable to centrally condensed morphologies, and should not apply to the many regions showing extended or diffuse morphologies, or exhibiting multiple peaks. Nevertheless, the observation that most virial masses are within a factor of two of the LTE mass suggests that in most of the clouds, the gravitational energy dominates the kinetic energy, and that most of the clouds are gravitationally bound.

Larson (1981) found that molecular clouds exhibit a well defined relationship between cloud size and average linewidth. In figure 24, we display the size-linewidth relation for the C¹⁸O 1–0 transition in our sample of regions. This transition should give the most accurate relation because it is unaffected by optical depth effects like the ¹³CO 1–0, but encloses all of the emission, unlike the C¹⁸O 2–1. We find considerable scatter compared to Larson’s relation; however, we cover only an order of magnitude in core size, much smaller than the three orders of magnitude considered by Larson. The scatter may also be increased due to the method we used to calculate the size of the region, which is primarily applicable to clouds showing a circular symmetry.

Figure 23a shows the average C¹⁸O 2–1 linewidth plotted against FIR luminosity. There is a 3.7σ correlation between linewidth and luminosity. This is not due to a correlation with distance, as is indicated in fig. 23b – the significance of the correlation between linewidth and distance is only 1.8σ .

5. Summary

We have begun a program of multi-wavelength observations which, when combined with existing infrared and optical data will yield detailed information about both the stars and their surrounding gas in a large sample of young stellar clusters within 1 kpc of the sun. Here we presented millimeter spectral line maps of a sample of 30 of these cluster-forming regions in the 1–0 transitions of ^{13}CO and C^{18}O . Smaller regions surrounding 17 of these sources were also mapped in the C^{18}O 2–1 transition. Based on our ^{13}CO 1–0 maps and the location of the stellar or protostellar source we proposed a sequence for the morphology of gas surrounding the clusters. The youngest sources have centrally condensed cores containing an embedded source, while the more evolved sources have extended or diffuse molecular gas. Optically visible Herbig Ae/Be stars associated with these sources are often located in cavities, suggestive that these types of stars can be responsible for the dispersal of molecular gas in cluster-forming regions.

We determined cloud masses independently using the three observed ^{13}CO and C^{18}O transitions, and compared the cloud properties derived from each of the three tracers in order to better understand systematic uncertainties in determining masses and linewidths. We found good consistency between the LTE and LVG methods, and between the masses and linewidths derived from C^{18}O 1–0 and 2–1. Virial masses were found to be within a factor of two of the LTE mass in most of the regions, suggesting that the gravitational energy dominates the kinetic energy in these regions, and that they are gravitationally bound.

Fits images of the integrated emission will be made available for general use via the project website. Our final data set will include sensitive ground based wide-field near-infrared imaging and spectroscopy, millimeter spectral-line and continuum maps and mid-infrared observations obtained with SIRTf. Once complete, it will be made available to the community via a web-based database, providing an invaluable resource for future star-formation studies.

FCRAO is supported by NSF grant AST 01-00793. This work is based in part on measurements made with the Heinrich-Hertz telescope, which is operated by the Submillimeter Telescope Observatory on behalf of Steward Observatory and the Max Planck Institut für Radioastronomie. This work made use of the NASA/IPAC Infrared Science Archive, which is operated by the Jet Propulsion Laboratory, California Institute of Technology, under contract with the National Aeronautics and Space Administration. We thank R. Gutermuth and D. Peterson for assistance with the FCRAO observing.

A. Individual Sources

In this section we give a brief summary of previous observations of each of the groups and clusters. For clarity we give a selection of just the most recent references on each source.

A.1. Class I

A.1.1. *BD+40°4124*

The Herbig Be star BD+40°4124 is the most massive member of a small group of young emission line stars (Hillenbrand et al. 1995), and a large number of highly embedded stars detected in the infrared by Palla et al. (1995). There is also a small molecular outflow in the region, probably driven by the embedded source V1318S (Palla et al. 1995).

A.1.2. *S 131*

S 131, also called Ceph OB Cloud 37 is a bright-rimmed cloud associated with an HII region (Sugitani, Fukui, & Ogura 1991) and the Galactic open cluster IC 1396. A small cluster was observed in this region by Sugitani et al. (1995), and several H α emission-line stars were detected by Ogura, Sugitani, & Pickles (2002). Interferometric C¹⁸O observations of this region were made by Sugitani et al. (1997).

A.1.3. *S 140*

The S 140 region is a prototypical cometary globule, photoionised on the south-west side by the B0 star HD 211880. It contains at least three bright infrared sources. A high-velocity molecular outflow was detected in ¹²CO observations by Snell et al. (1984). Previous smaller scale molecular line observations have been made by Minchin, White, & Padman (1993) who determined that the outflow was driven by the source IRS 1.

A.1.4. *L 1206*

L 1206 is a bright-rimmed globule associated with the HII region S 145. It has a molecular outflow, discovered in a survey by Sugitani et al. (1989).

A.1.5. Cep A

The Cepheus A region is a molecular cloud containing a very active star forming region indicated by a powerful molecular outflow (Rodríguez, Moran, & Ho 1980b), more than 25 water masers (Torrelles et al. 1996) and numerous thermal and non-thermal radio sources (Hughes 2001; Garay et al. 1996).

A.1.6. AFGL 490

AFGL 490 is a relatively isolated infrared source in the Cam OB1 complex (Chini, Henning, & Pfau 1991). It is a young massive star-forming region, containing a cluster of embedded sources (Hodapp 1994) and associated with a molecular outflow (Snell et al. 1984), and maser emission (Henkel, Guesten, & Haschick 1986).

A.1.7. GGD 4

GGD 4 contains a small cluster of young stars (Hodapp 1994) and the driving source of a molecular outflow (Fukui 1989).

A.1.8. CB 34

CB34 is a relatively distant large globule containing a small group of infrared sources (Alves & Yun 1995), at least two high-velocity jets (Khazadyan et al. 2002) and several millimeter continuum sources thought to be very young protostars (Huard, Weintraub, & Sandell 2000).

A.1.9. Mon R2

This is an association of B1-B9 stars located in the Mon R2 giant molecular cloud. It is a very active star-forming region, associated with a powerful molecular outflow (Bally & Lada 1983; Tafalla et al. 1997), a compact HII region (Wood & Churchwell 1989), an infrared cluster (Carpenter 2000), and OH masers (Minier et al. 2001).

A.1.10. GGD 12-15

GGD 12–15 is an active star-forming region embedded in the Monoceros molecular cloud. It is associated with a strong water maser, a cometary compact HII region (Rodríguez et al. 1978, 1980a; Gomez et al. 1998), several millimeter-continuum sources and a bipolar CO outflow (Little, Heaton, & Dent 1990).

A.1.11. NGC 2264

The NGC 2264 region in northern Monoceros contains two well studied star formation regions, IRS 1 and IRS 2. Thirty IRAS sources, most classified as Class I protostars (Margulis, Lada, & Young 1989) are present, as well as ~ 360 near-infrared sources (Lada, Young, & Greene 1993). At least nine molecular outflow sources were identified in an unbiased survey by Margulis & Lada (1986).

A.2. Class II

A.2.1. IRAS 20050

The region IRAS 20050 contains an embedded star and an extremely-high-velocity (EHV) molecular jet and multipolar molecular outflow, likely the superposition of outflows from several young stars (Bachiller, Fuente, & Tafalla 1995).

A.2.2. S 106

The S 106 region contains a bipolar HII region and an associated molecular cloud. Near-infrared observations by Hodapp & Rayner (1991) revealed a cluster of 160 young stars in this region. A recent much deeper near-infrared survey of the region suggests that the total number of young stars could be much greater (~ 600) (Oasa et al. 2002). CO observations of this region were made by Schneider et al. (2002).

A.2.3. NGC 7129

NGC 7129 is a reflection nebula in the region of a young cluster, containing three B-type stars (BD+65°1638, BD+65°1637 and LkH α 234) and several embedded infrared sources. It

is associated with Herbig-Haro objects and several molecular outflows (Font, Mitchell, & Sandell 2001, and refs. therein). Submillimeter continuum observations by Font et al. (2001) reveal several sources which they interpret as prestellar. FMBRP have made higher-resolution ^{13}CO and C^{18}O 1–0 observations of the molecular gas in a small portion of this region, finding a cavity surrounding BD+65°1637, while LkH α 234 is located at the peak of ^{13}CO emission. Molecular line observations of the region were also made by Miskolczi et al. (2001).

A.2.4. S 140-N

The region S 140-N contains a molecular outflow, discovered by Fukui et al. (1986). Davis et al. (1998) made a higher resolution ^{12}CO 2–1 map of the outflow and determined that it is powered by the intermediate-luminosity IRAS source 22178+6317. To the east of the molecular outflow source are a sequence of Herbig-Haro objects (HH 251-254) oriented in a northwest-southeast direction indicating a second outflow (Eiroa et al. 1993).

A.2.5. L 1211

L 1211 is a dense core in the Cepheus cloud complex. It contains a very young cluster, detected in millimeter continuum observations by Tafalla et al. (1999), and powers two molecular outflows.

A.2.6. Cep C

The Cepheus C region is an isolated core within the Cepheus OB3 molecular cloud (Sargent 1977). The region contains a cluster of infrared sources (Hodapp 1994) and is associated with water maser emission (Wouterloot & Walmsley 1986) and an outflow (Fukui 1989).

A.2.7. S 171

S 171 is a bright-rimmed cloud associated with the Cepheus OB4 stellar association, an actively star-forming HII region, and molecular cloud complex (Yang & Fukui 1992). The main heating and ionizing source of this region is believed to be the star cluster, Be 59 (Okada et al. 2002). Several H α emission-line stars were detected in this region by Ogura

et al. (2002).

A.2.8. NGC 1333

NGC 1333 is a reflection nebula associated with a region of recent, extremely active star formation in the Perseus molecular cloud. A cluster of about 150 low- to intermediate-mass YSOs have been identified in near-infrared images (Aspin, Sandell, & Russell 1994). The region also contains about 20 groups of Herbig-Haro objects, some with highly collimated jets (Bally, Devine, & Reipurth 1996). Rodríguez, Anglada, & Curiel (1999) found a total of 44 sources at centimeter wavelengths, most of which are associated or believed to be associated with young stellar objects in the region.

A.2.9. L 1551

L 1551 is a compact molecular cloud located in the southern part of the Taurus region. It shows abundant signs of ongoing star-formation, and contains the infrared source IRS 5, probably the most well-studied low-mass young stellar object in the galaxy. IRS 5 powers a powerful well-collimated bipolar molecular outflow (e.g. Moriarty-Schieven & Snell 1988), and is associated with several Herbig-Haro objects. Also in the region are several other overlapping molecular outflows and a number of T-Tauri stars (including the well-known sources HL Tau and XZ Tau).

A.2.10. VY Mon

VY Mon is a highly-reddened Herbig Be star in the Mon OB1 region. It is located 85'' south of the reflection nebula IC 446.

A.3. Class III

A.3.1. MWC 297

MWC 297 is an extremely reddened Herbig Be star (Drew et al. 1997) seen in projection against the HII region S 62, although its relationship to the HII region is not clear. FMBRP have made higher-resolution ^{13}CO and C^{18}O 1–0 observations of a small region surrounding

this source. Their observations show evidence for a cavity surrounding the star, within a more diffuse molecular gas environment.

A.3.2. VV Ser

VV Ser was determined to be a Herbig Ae star by Testi et al. (1998). A small region surrounding this star was mapped in ^{13}CO and C^{18}O 1–0 at higher resolution by FMBRP. They detected very little molecular gas in the vicinity of this star, and interpreted that it was located in a cavity.

A.3.3. HD 200775

HD 200775 is a B3 star located at the northern edge of an elongated molecular cloud. It is the illuminating star of the well-known reflection nebula NGC 7023 and is associated with a bipolar outflow (Watt et al. 1986) and a cluster of $\text{H}\alpha$ emission-line stars (Urban et al. 2001). The region has been previously mapped in ^{13}CO 1–0 by Fuente et al. (1998b) and FMBRP. These observations show that the star is located within a biconical cavity, that has probably been excavated by a bipolar outflow. However Fuente et al. (1998b) found no evidence for current high velocity gas within the lobes of the cavity.

A.3.4. L 988-e

The L 988-e cloud contains a cluster of bright infrared sources (Hodapp 1994) coinciding with the position of a molecular outflow (Clark 1986).

A.3.5. IC 5146

IC 5146 is a young stellar cluster, associated with a reflection nebula illuminated by the B0 V star BD+46°3474. Also embedded in the same cloud is the HAeBe variable BD+46°3471 and ~ 100 $\text{H}\alpha$ emission-line stars (Herbig & Dahm 2002).

A.3.6. HD 216629

HD 216629 is a Be star in the Cepheus cloud with a close companion (Pirzkal, Spillar, & Dyck 1997) and surrounded by a cluster of infrared sources (Testi et al. 1998). Fuente et al. (1998a, 2002) have made ^{13}CO 1–0, C^{18}O 1–0 and CO 2–1 observations of a 1 pc region surrounding this star. They detected very little molecular gas, as traced by ^{13}CO close to the star. They describe the gas morphology in this source as a cavity.

A.3.7. IC 348

The young cluster IC 348 is located in the Perseus molecular cloud. As well as ~ 40 optically visible stars, including the B5 V star BD+31°643 (associated with a well-known reflection nebula), and 16 $\text{H}\alpha$ emission-line stars, it contains almost 400 embedded stars, detected in the near-infrared by Lada & Lada (1995). High-resolution ^{13}CO and C^{18}O observations were made over a small portion of this region by Bachiller et al. (1987).

A.3.8. LkH α 101

LkH α 101 is a bright Herbig Ae/Be star associated with a powerful ionised stellar wind, extended HII region and reflection nebulosity (Barsony et al. 1991). Ungerechts & Thaddeus (1987) associated this star with an extension of the Perseus cloud, and the region containing XY Per. Using an analysis of the reddening of Hipparcos stars A. Wilson (2002, personal communication) determined a distance of 280 pc to this complex. We therefore adopt this distance, rather than the value of 800 pc quoted in the literature.

A.3.9. XY Per

XY Per is a Herbig Be star surrounded by a small cluster of infrared sources (Testi et al. 1997). It is located in the same molecular cloud as LkH α 101 (Ungerechts & Thaddeus 1987).

REFERENCES

- Adams, F. C. & Myers, P. C. 2001, *ApJ*, 553, 744
- Alves, J. F. & Yun, J. L. 1995, *ApJ*, 438, L107
- Aspin, C. & Barsony, M. 1994, *A&A*, 288, 849
- Aspin, C., Sandell, G., & Russell, A. P. G. 1994, *A&AS*, 106, 165
- Bachiller, R., Fuente, A., & Tafalla, M. 1995, *ApJ*, 445, L51
- Bachiller, R., Guilloteau, S., & Kahane, C. 1987, *A&A*, 173, 324
- Bally, J., Devine, D., & Reipurth, B. 1996, *ApJ*, 473, L49
- Bally, J. & Lada, C. J. 1983, *ApJ*, 265, 824
- Barsony, M., Schombert, J. M., & Kis-Halas, K. 1991, *ApJ*, 379, 221
- Bergin, E. A., Alves, J., Huard, T., & Lada, C. J. 2002, *ApJ*, 570, L101
- Carkner, L., Feigelson, E. D., Koyama, K., Montmerle, T., & Reid, I. N. 1996, *ApJ*, 464, 286
- Carpenter, J. M. 2000, *AJ*, 120, 3139
- . 2002, *AJ*, 124, 1593
- Carpenter, J. M., Snell, R. L., & Schloerb, F. P. 1990, *ApJ*, 362, 147
- . 1995, *ApJ*, 445, 246
- Casoli, F., Combes, F., Dupraz, C., Gerin, M., & Boulanger, F. 1986, *A&A*, 169, 281
- Chen, H., Tafalla, M., Greene, T. P., Myers, P. C., & Wilner, D. J. 1997, *ApJ*, 475, 163
- Chini, R., Henning, T., & Pfau, W. 1991, *A&A*, 247, 157
- Clark, F. O. 1986, *A&A*, 164, L19
- Davis, C. J., Moriarty-Schieven, G., Eisloffel, J., Hoare, M. G., & Ray, T. P. 1998, *AJ*, 115, 1118
- Drew, J. E., Busfield, G., Hoare, M. G., Murdoch, K. A., Nixon, C. A., & Oudmaijer, R. D. 1997, *MNRAS*, 286, 538

- Eiroa, C., Lenzen, R., Miranda, L. F., Torrelles, J. M., Anglada, G., & Estalella, R. 1993, *AJ*, 106, 613
- Evans, N. J., Mundy, L. G., Kutner, M. L., & Depoy, D. L. 1989, *ApJ*, 346, 212
- Font, A. S., Mitchell, G. F., & Sandell, G. . 2001, *ApJ*, 555, 950
- Fridlund, M., Hultgren, M., & Liseau, R. 1997, in *IAU Symposium*, Vol. 182, 19–28
- Fuente, A., Martín-Pintado, J., Bachiller, R., Neri, R., & Palla, F. 1998a, *A&A*, 334, 253
- Fuente, A., Martín-Pintado, J., Bachiller, R., Rodríguez-Franco, A., & Palla, F. 2002, *A&A*, 387, 977
- Fuente, A., Martín-Pintado, J., Rodríguez-Franco, A., & Moriarty-Schieven, G. D. 1998b, *A&A*, 339, 575
- Fukui, Y. 1989, in *Low Mass Star Formation and Pre-main Sequence Objects*, 95
- Fukui, Y., Sugitani, K., Takaba, H., Iwata, T., Mizuno, A., Ogawa, H., & Kawabata, K. 1986, *ApJ*, 311, L85
- Garay, G., Ramirez, S., Rodríguez, L. F., Curiel, S., & Torrelles, J. M. 1996, *ApJ*, 459, 193
- Goldsmith, P. F., Bergin, E. A., & Lis, D. C. 1997, *ApJ*, 491, 615
- Gomez, Y., Lebron, M., Rodriguez, L. F., Garay, G., Lizano, S., Escalante, V., & Canto, J. 1998, *ApJ*, 503, 297
- Henkel, C., Guesten, R., & Haschick, A. D. 1986, *A&A*, 165, 197
- Herbig, G. H. & Dahm, S. E. 2002, *AJ*, 123, 304
- Heyer, M. H., Narayanan, G., & Brewer, M. K. 2001, *On the Fly Mapping at the FCRAO 14m Telescope*, FCRAO
- Hillenbrand, L. A. 1997, *AJ*, 113, 1733
- Hillenbrand, L. A., Meyer, M. R., Strom, S. E., & Skrutskie, M. F. 1995, *AJ*, 109, 280
- Hodapp, K. 1994, *ApJS*, 94, 615
- Hodapp, K. & Rayner, J. 1991, *AJ*, 102, 1108
- Huard, T. L., Weintraub, D. A., & Sandell, G. 2000, *A&A*, 362, 635

- Hughes, V. A. 2001, *ApJ*, 563, 919
- Jijina, J., Myers, P. C., & Adams, F. C. 1999, *ApJS*, 125, 161
- Khanzadyan, T., Smith, M. D., Gredel, R., Stanke, T., & Davis, C. J. 2002, *A&A*, 383, 502
- Kutner, M. L. & Ulich, B. L. 1981, *ApJ*, 250, 341
- Lada, C. J., Alves, J., & Lada, E. A. 1996, *AJ*, 111, 1964
- . 1999, *ApJ*, 512, 250
- Lada, C. J., Young, E. T., & Greene, T. P. 1993, *ApJ*, 408, 471
- Lada, E. A. 1992, *ApJ*, 393, L25
- Lada, E. A., Bally, J., & Stark, A. A. 1991, *ApJ*, 368, 432
- Lada, E. A. & Lada, C. J. 1995, *AJ*, 109, 1682
- Larson, R. B. 1981, *MNRAS*, 194, 809
- Little, L. T., Heaton, B. D., & Dent, W. R. F. 1990, *A&A*, 232, 173
- MacLaren, I., Richardson, K. M., & Wolfendale, A. W. 1988, *ApJ*, 333, 821
- Margulis, M. & Lada, C. J. 1986, *ApJ*, 309, L87
- Margulis, M., Lada, C. J., & Young, E. T. 1989, *ApJ*, 345, 906
- Minchin, N. R., White, G. J., & Padman, R. 1993, *A&A*, 277, 595
- Minier, V., Conway, J. E., & Booth, R. S. 2001, *A&A*, 369, 278
- Miskolczi, B., Tothill, N. F. H., Mitchell, G. F., & Matthews, H. E. 2001, *ApJ*, 560, 841
- Moriarty-Schieven, G. H. & Snell, R. L. 1988, *ApJ*, 332, 364
- Oasa, Y., Tamura, M., Nakajima, Y., & Itoh, Y. 2002, in *The Proceedings of the IAU 8th Asian-Pacific Regional Meeting, Volume II*. Edited by S. Ikeuchi, J. Hearnshaw, and T. Hanawa, the Astronomical Society of Japan, p. 189–190
- Ogura, K., Sugitani, K., & Pickles, A. 2002, *AJ*, 123, 2597
- Okada, Y., Onaka, T., Shibai, H., & Doi, Y. 2002, in *Exploiting the ISO Data Archive. Infrared Astronomy in the Internet Age*. Edited by C. Gry et al.

- Onishi, T., Mizuno, A., Kawamura, A., Ogawa, H., & Fukui, Y. 1996, *ApJ*, 465, 815
- Palla, F. & Stahler, S. W. 2000, *ApJ*, 540, 255
- Palla, F., Testi, L., Hunter, T. R., Taylor, G. B., Prusti, T., Felli, M., Natta, A., & Stanga, R. M. 1995, *A&A*, 293, 521
- Pirzkal, N., Spillar, E. J., & Dyck, H. M. 1997, *ApJ*, 481, 392
- Rodríguez, L. F., Anglada, G., & Curiel, S. 1999, *ApJS*, 125, 427
- Rodríguez, L. F., Moran, J. M., Dickinson, D. F., & Gyulbudagian, A. L. 1978, *ApJ*, 226, 115
- Rodríguez, L. F., Moran, J. M., Gottlieb, E. W., & Ho, P. T. P. 1980a, *ApJ*, 235, 845
- Rodríguez, L. F., Moran, J. M., & Ho, P. T. P. 1980b, *ApJ*, 240, L149
- Rohlfs, K. & Wilson, T. L. 2000, *Tools of Radio Astronomy*, 3rd edn. (Springer-Verlag)
- Sargent, A. I. 1977, *ApJ*, 218, 736
- Schneider, N., Simon, R., Kramer, C., Stutzki, J., & Bontemps, S. 2002, *A&A*, 384, 225
- Schreyer, K., Helmich, F. P., van Dishoeck, E. F., & Henning, T. 1997, *A&A*, 326, 347
- Snell, R. L., Scoville, N. Z., Sanders, D. B., & Erickson, N. R. 1984, *ApJ*, 284, 176
- Sugitani, K., Fukui, Y., Mizuni, A., & Ohashi, N. 1989, *ApJ*, 342, L87
- Sugitani, K., Fukui, Y., & Ogura, K. 1991, *ApJS*, 77, 59
- Sugitani, K., Morita, K., Nakano, M., Tamura, M., & Ogura, K. 1997, *ApJ*, 486, L141
- Sugitani, K., Tamura, M., & Ogura, K. 1995, *ApJ*, 455, L39
- Tafalla, M., Bachiller, R., Wright, M. C. H., & Welch, W. J. 1997, *ApJ*, 474, 329
- Tafalla, M., Myers, P. C., Mardones, D., & Bachiller, R. 1999, *A&A*, 348, 479
- Testi, L., Palla, F., & Natta, A. 1998, *A&AS*, 133, 81
- . 1999, *A&A*, 342, 515
- Testi, L., Palla, F., Prusti, T., Natta, A., & Maltagliati, S. 1997, *A&A*, 320, 159
- Tieftrunk, A. R., Megeath, S. T., Wilson, T. L., & Rayner, J. T. 1998, *A&A*, 336, 991

- Torrelles, J. M., Gomez, J. F., Rodríguez, L. F., Curiel, S., Ho, P. T. P., & Garay, G. 1996, *ApJ*, 457, L107
- Ungerechts, H. & Thaddeus, P. 1987, *ApJS*, 63, 645
- Urban, A., Meyer, M. R., Herbig, G. H., & Dahm, S. 2001, American Astronomical Society Meeting, 199
- Watt, G. D., Burton, W. B., Choe, S.-U., & Liszt, H. S. 1986, *A&A*, 163, 194
- Wood, D. O. S. & Churchwell, E. 1989, *ApJS*, 69, 831
- Wouterloot, J. G. A. & Walmsley, C. M. 1986, *A&A*, 168, 237
- Yang, J. & Fukui, Y. 1992, *ApJ*, 386, 618

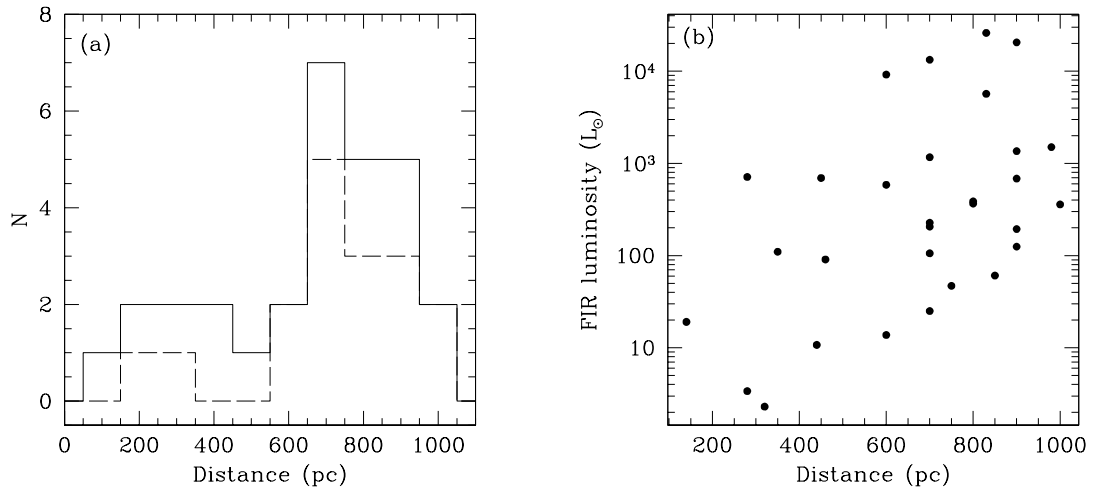


Fig. 1.— (a) Histogram of number of sources with distance. The solid line indicates the full sample, and the dashed line those sources for which all three lines were observed. (b) FIR luminosity vs. distance for all the sources in the sample.

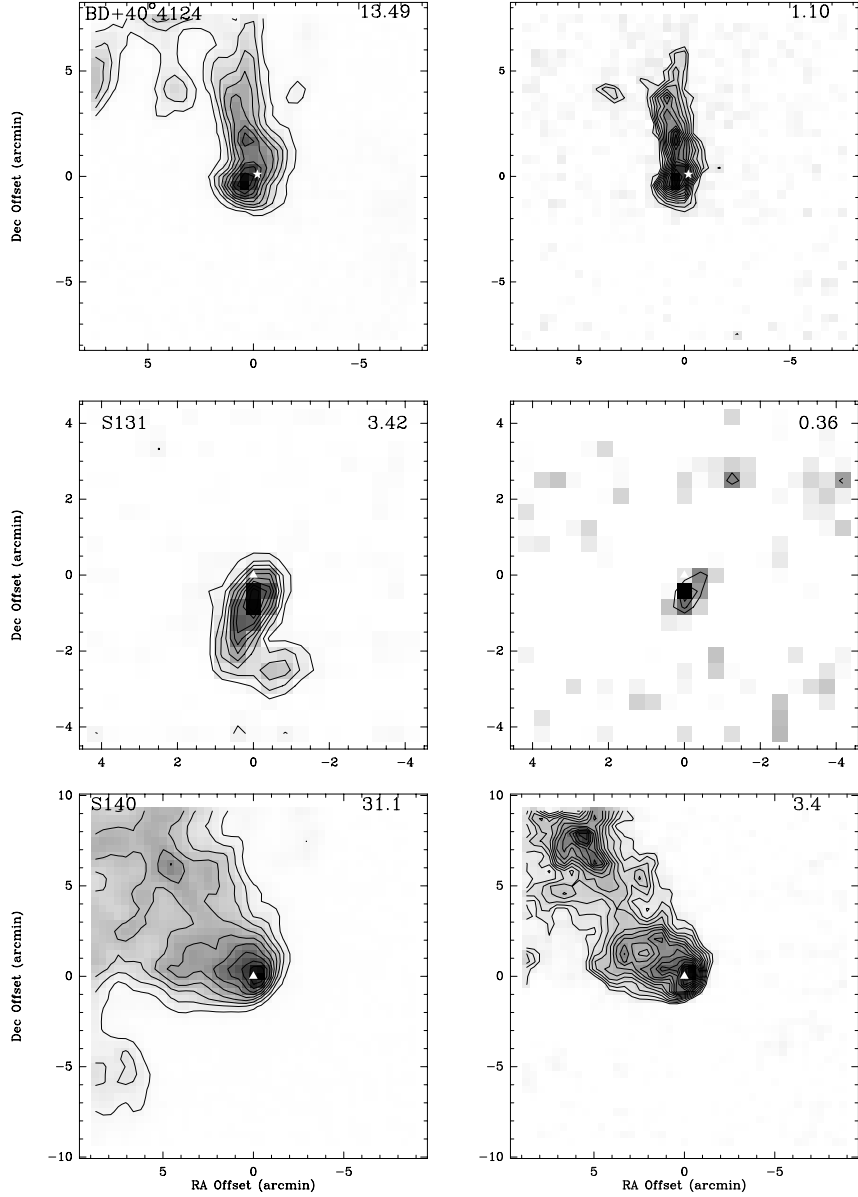


Fig. 2.— Integrated intensity maps of BD+40°4124 (top) and S131 (middle) and S140 (bottom), all classified as developmental Class I. The value of the maximum integrated intensity in K km s^{-1} is given in the top right corner of each panel. Left panels show ^{13}CO 1–0 integrated emission, with contours at 10% intervals from 10% to 100% of the maximum integrated intensity. Right panels show integrated C^{18}O 1–0 emission. Base contour is 3σ , contour interval is 1σ , except for S131 where the base contour is at 2σ and contour intervals at 0.5σ . (0,0) positions are as given in table 1. Triangles indicate the position of an IRAS or near-infrared (embedded) source and stars indicate the position of an optically visible Herbig Ae/Be star.

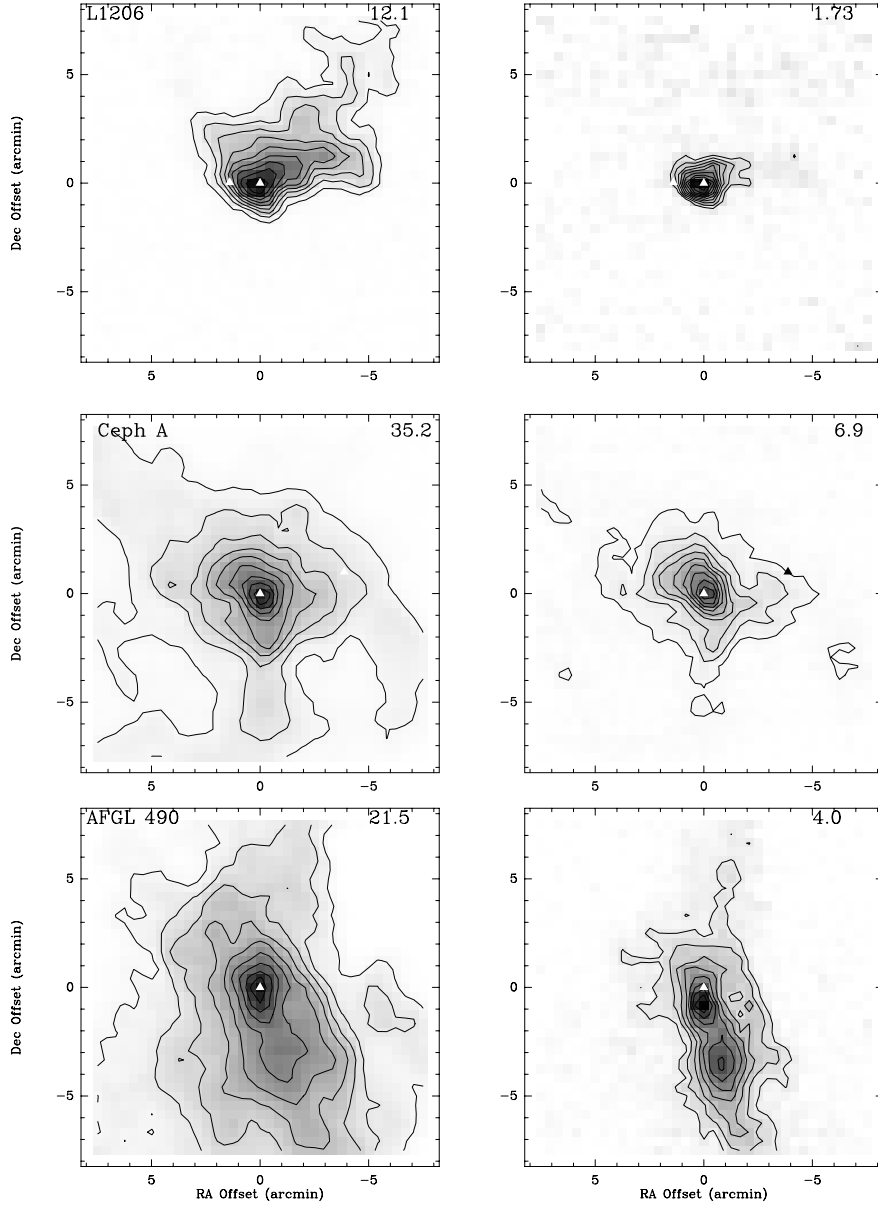


Fig. 3.— Integrated intensity maps of developmental Class I sources L 1206 (top), Cep A (middle) and AFGL 490 (bottom). The value of the maximum integrated intensity in K km s^{-1} is given in the top right corner of each panel. Left panels show ^{13}CO 1–0 integrated emission, with contours at 10% intervals from 10% to 100% of the maximum integrated intensity. Right panels show integrated C^{18}O 1–0 emission. Base contour is 3σ , contour interval is 10%, except for L 1206 where contour interval is 1σ . (0,0) positions are as given in table 1. Symbols as in figure 2.

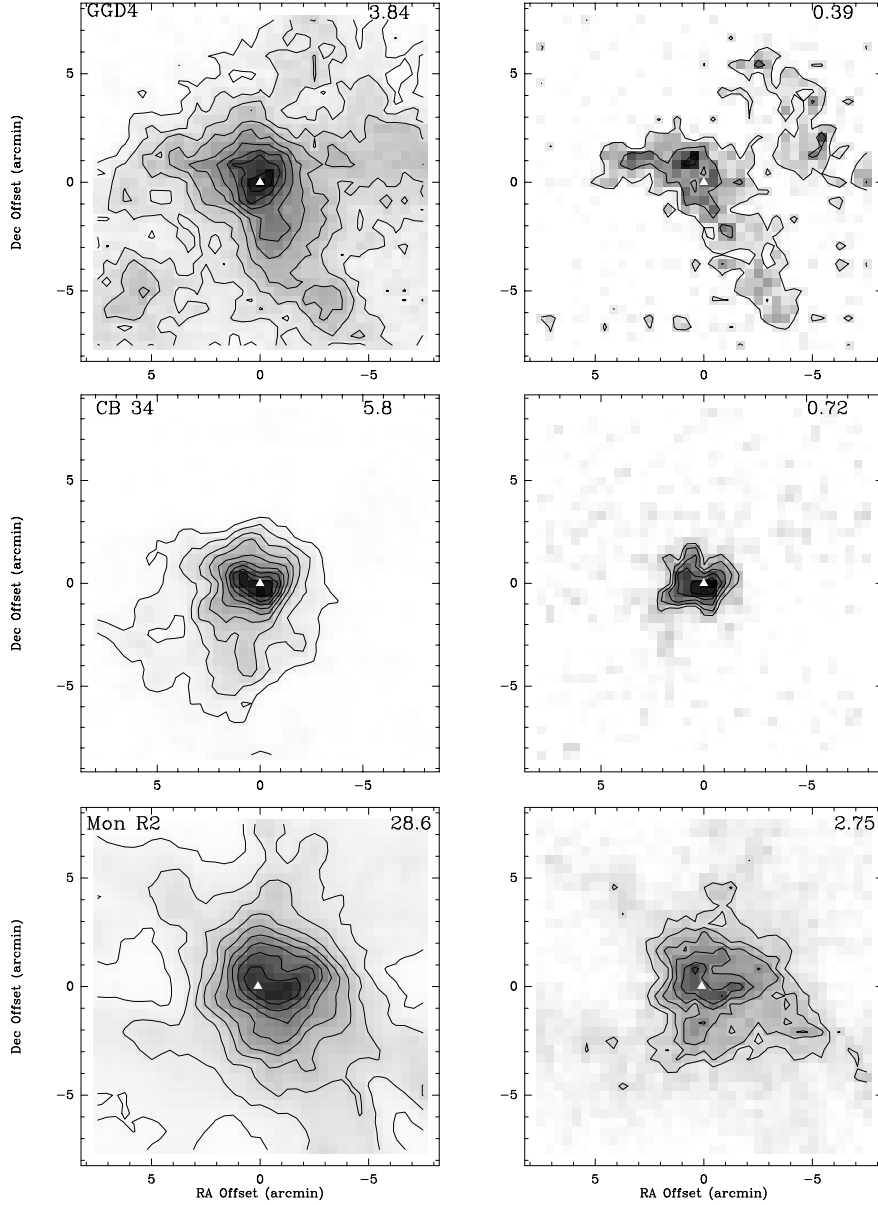


Fig. 4.— Integrated intensity maps of GGD 4 (top), CB34 (middle) and Mon R2 (bottom). The value of the maximum integrated intensity in K km s^{-1} is given in the top right corner of each panel. Left panels show ^{13}CO 1–0 integrated emission, with contours at 10% intervals from 10% to 100% of the maximum integrated intensity. Right panels show integrated C^{18}O 1–0 emission. Base contour is 3σ , contour interval is 1σ , except for GGD 4 where the base contour is at 1σ . (0,0) positions are as given in table 1. Symbols as in figure 2.

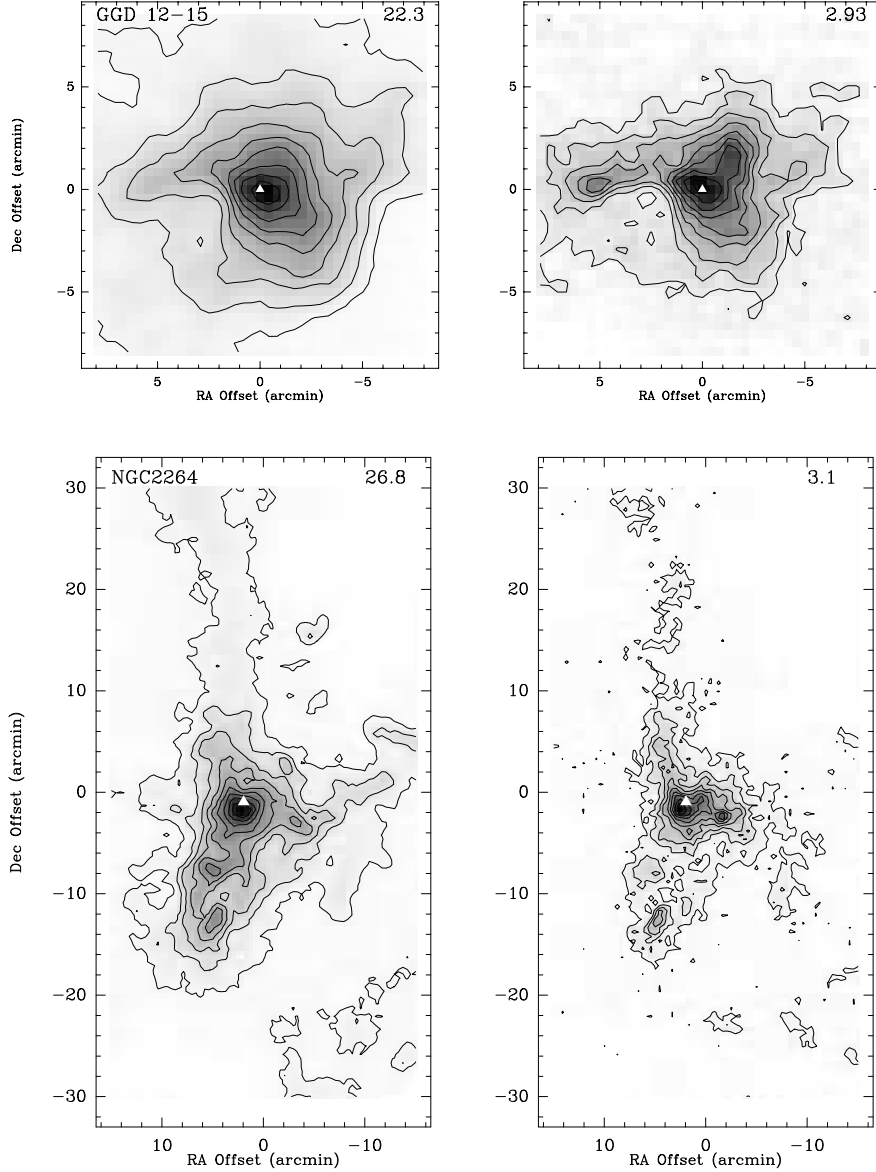


Fig. 5.— Integrated intensity maps of Class I sources GGD 12-15 (top) and NGC 2264 (bottom). The value of the maximum integrated intensity in K km s^{-1} is given in the top right corner of each panel. Left panel shows ^{13}CO 1-0 integrated emission, with contours at 10% intervals from 10% to 100% of the maximum integrated intensity. Right panel shows integrated C^{18}O 1-0 emission. Base contour is 3σ (10% for NGC 2264), contour interval is 1σ (10% for NGC 2264). (0,0) positions are as given in table 1. Symbols as in figure 2.

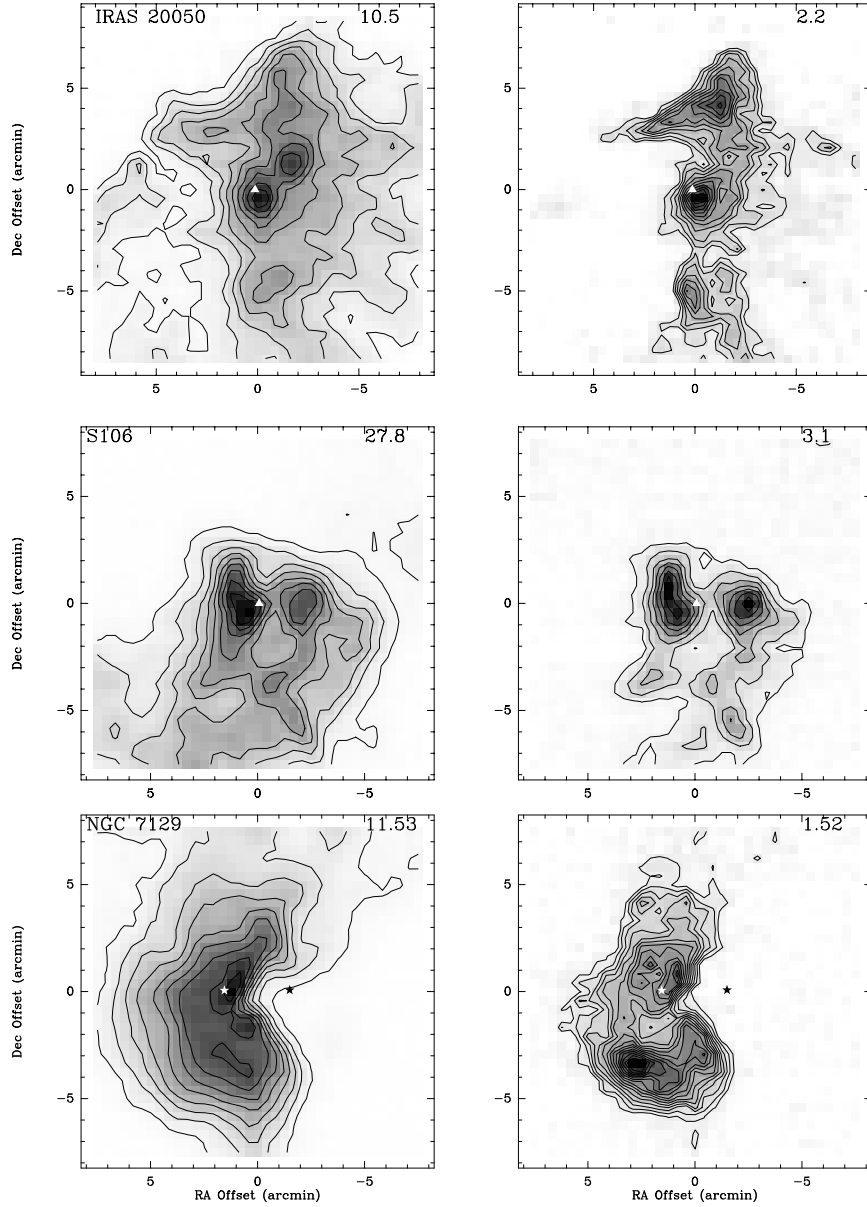


Fig. 6.— Integrated intensity maps of Class II sources IRAS 20050 (top), S 106 (middle) and NGC 7129 (bottom). The value of the maximum integrated intensity in K km s^{-1} is given in the top right corner of each panel. Left panels show ^{13}CO 1–0 integrated emission, with contours at 10% intervals from 10% to 100% of the maximum integrated intensity. Right panels show integrated C^{18}O 1–0 emission. Base contour is 3σ , contour interval is 1σ . (0,0) positions are as given in table 1. Symbols as in figure 2.

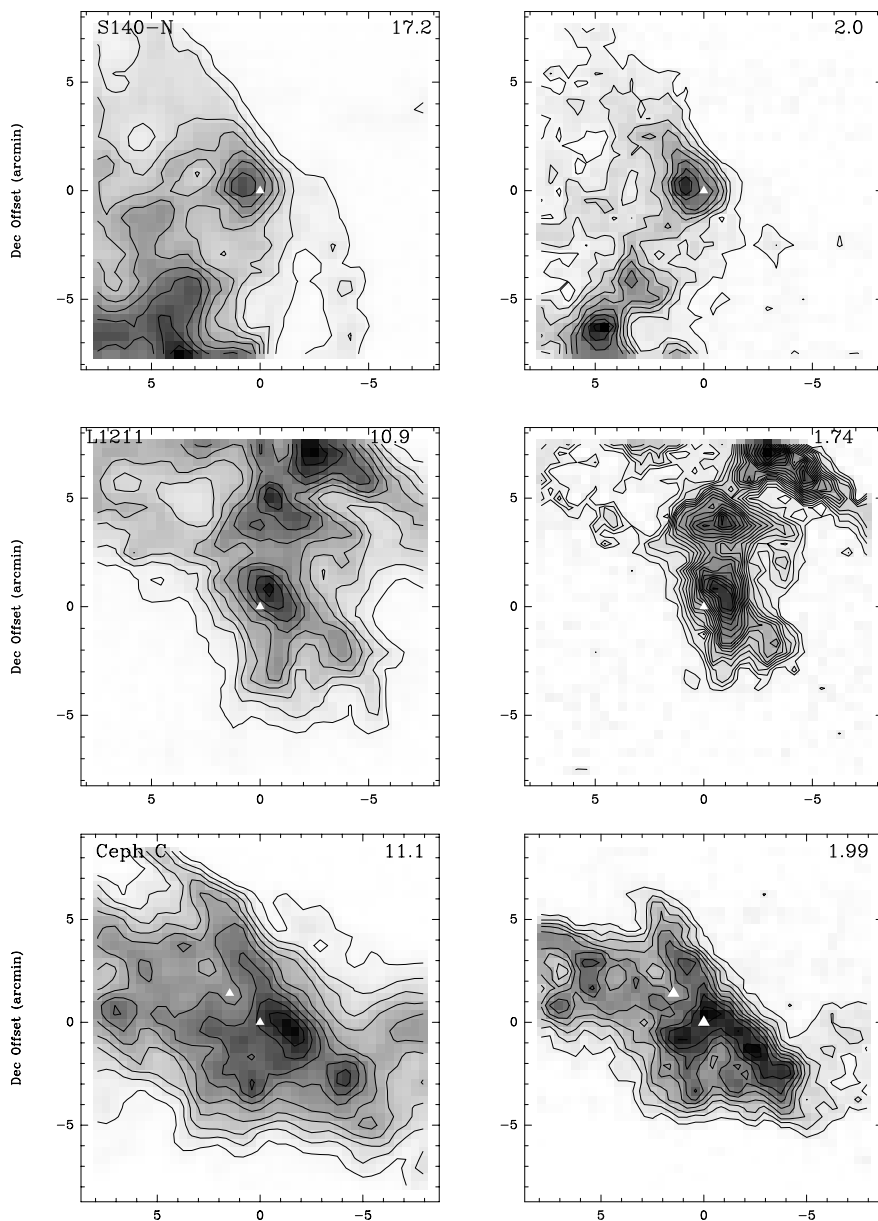


Fig. 7.— Integrated intensity maps of Class II sources S140-N (top), L1211 (middle) and Ceph C (bottom). The value of the maximum integrated intensity in K km s^{-1} is given in the top right corner of each panel. Left panels show ^{13}CO 1–0 integrated emission, with contours at 10% intervals from 10% to 100% of the maximum integrated intensity. Right panels show integrated C^{18}O 1–0 emission. Base contour is 3σ (10% for S140-N), contour interval is 1σ (10% for S140-N). (0,0) positions are as given in table 1. Symbols as in figure 2.

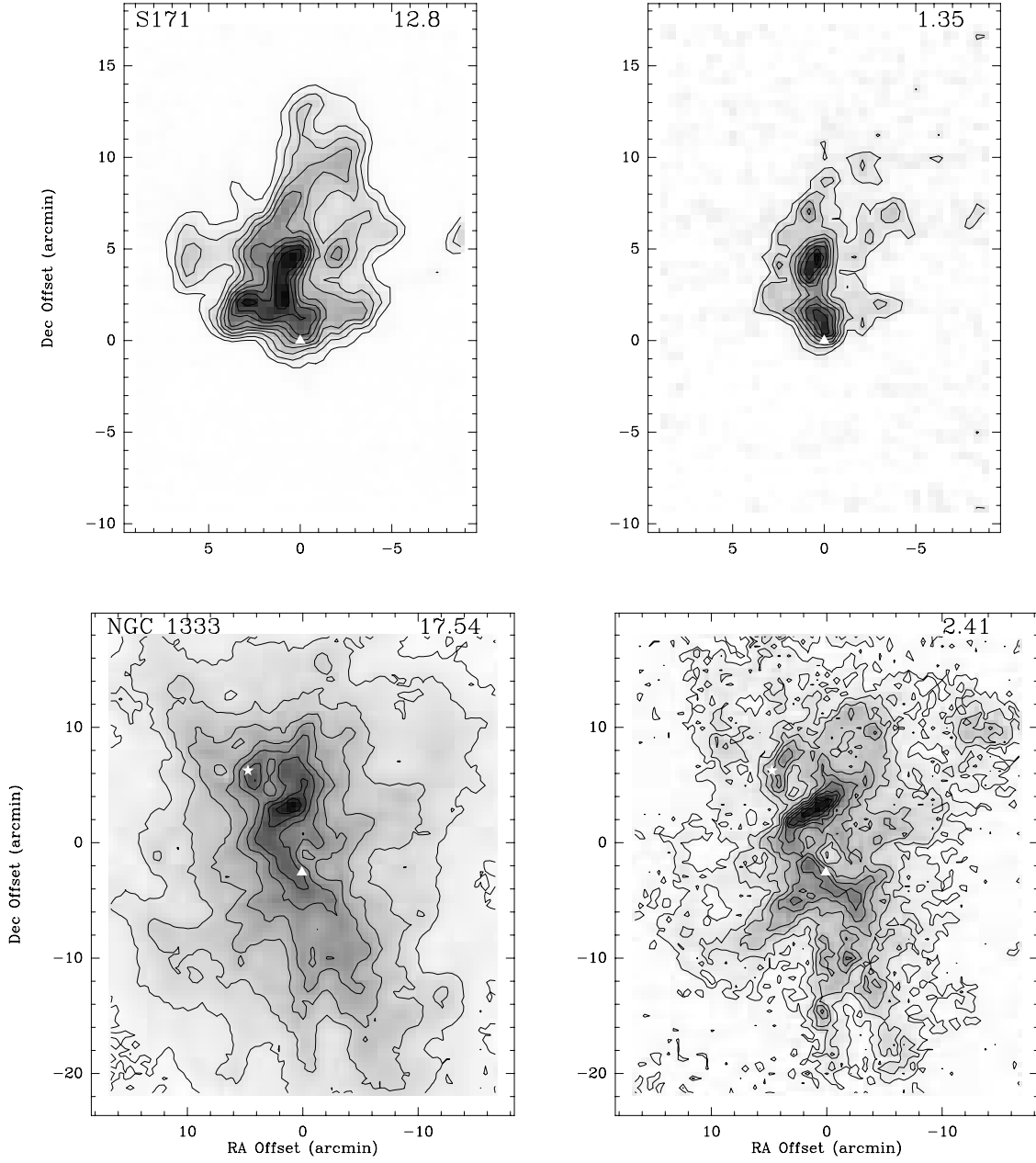


Fig. 8.— Integrated intensity maps of Class II sources S 171 (top) and NGC 1333 (bottom). The value of the maximum integrated intensity in K km s^{-1} is given in the top right corner of each panel. Left panels show ^{13}CO 1–0 integrated emission, with contours at 10% intervals from 10% to 100% of the maximum integrated intensity. Right panels show integrated C^{18}O 1–0 emission. Base contour is 3σ , contour interval is 1σ . (0,0) positions are as given in table 1. Symbols as in figure 2.

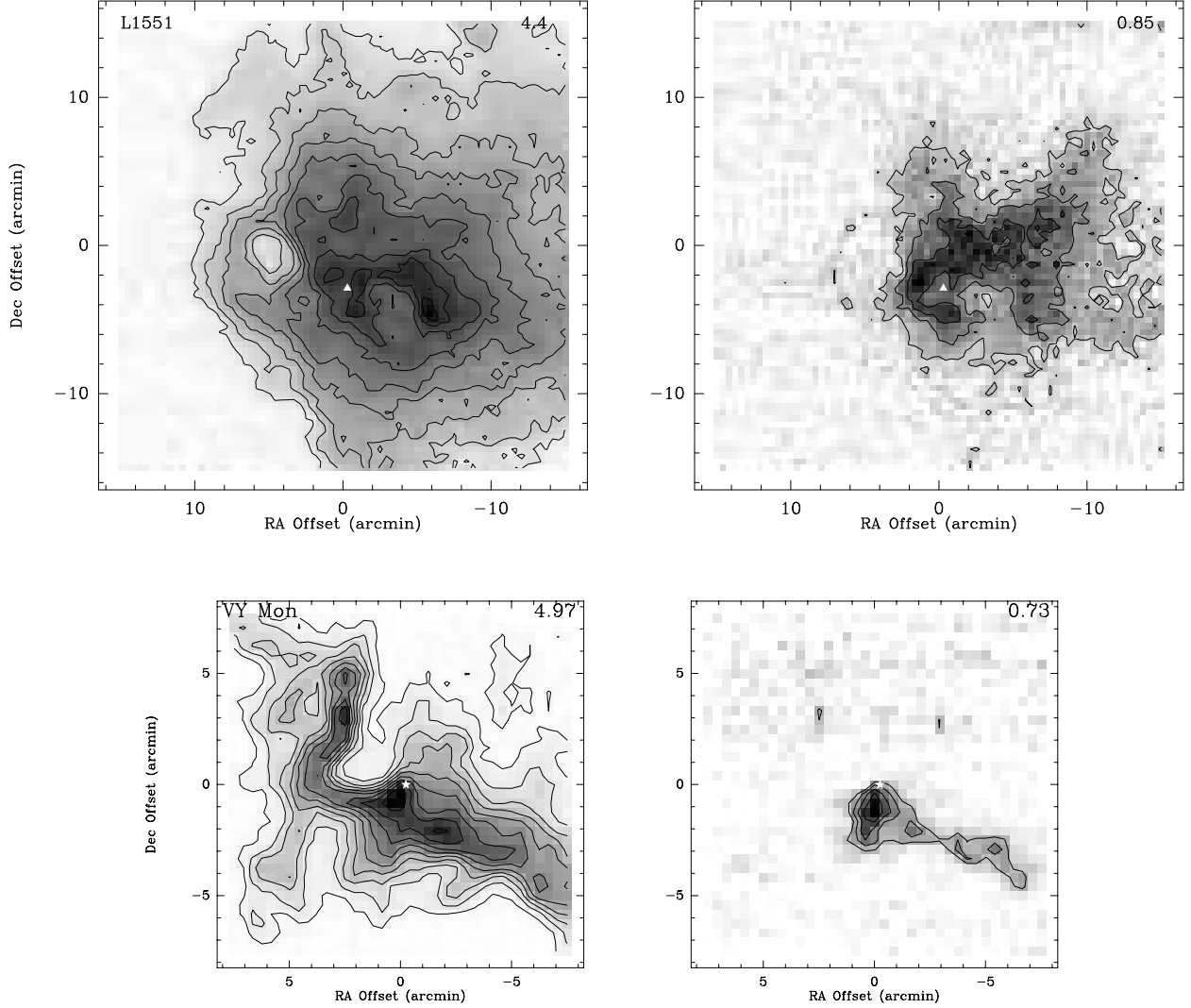


Fig. 9.— Integrated intensity maps of Class II sources L 1551 (top), and VY Mon (bottom). The value of the maximum integrated intensity in K km s^{-1} is given in the top right corner of each panel. Left panels show ^{13}CO 1–0 integrated emission, with contours at 10% intervals from 10% to 100% of the maximum integrated intensity. Right panels show integrated C^{18}O 1–0 emission. Base contour is 3σ (1σ for L1551), contour interval is 1σ . (0,0) positions are as given in table 1. Symbols as in figure 2.

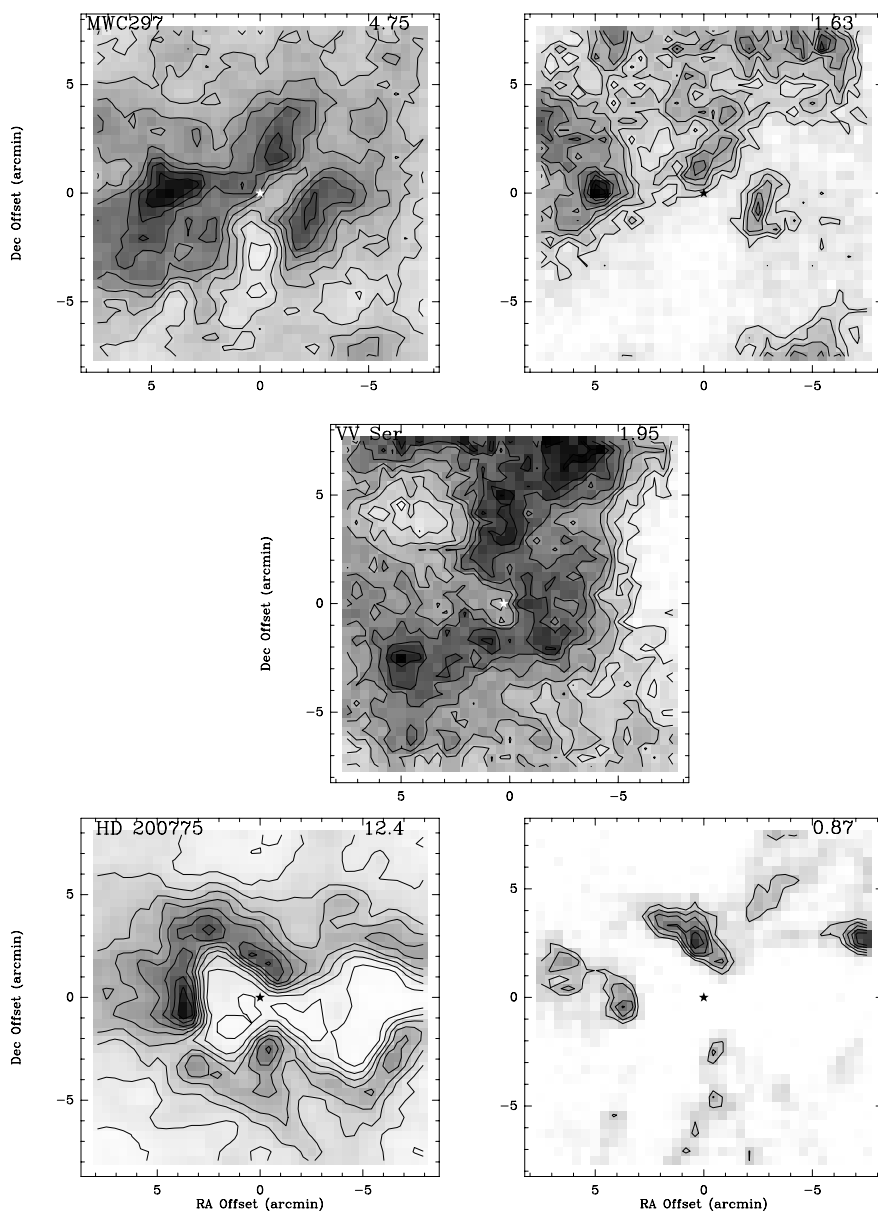


Fig. 10.— Integrated intensity maps of Class III sources MWC 297 (top), VV Ser (middle) and HD 200775 (bottom). The value of the maximum integrated intensity in K km s^{-1} is given in the top right corner of each panel. Left panels show ^{13}CO 1–0 integrated emission, with contours at 10% intervals from 10% to 100% of the maximum integrated intensity. Right panels show integrated C^{18}O 1–0 emission. Base contour is 3σ , contour interval is 1σ . C^{18}O emission was too weak to map in VV Ser. (0,0) positions are as given in table 1. Symbols as in figure 2.

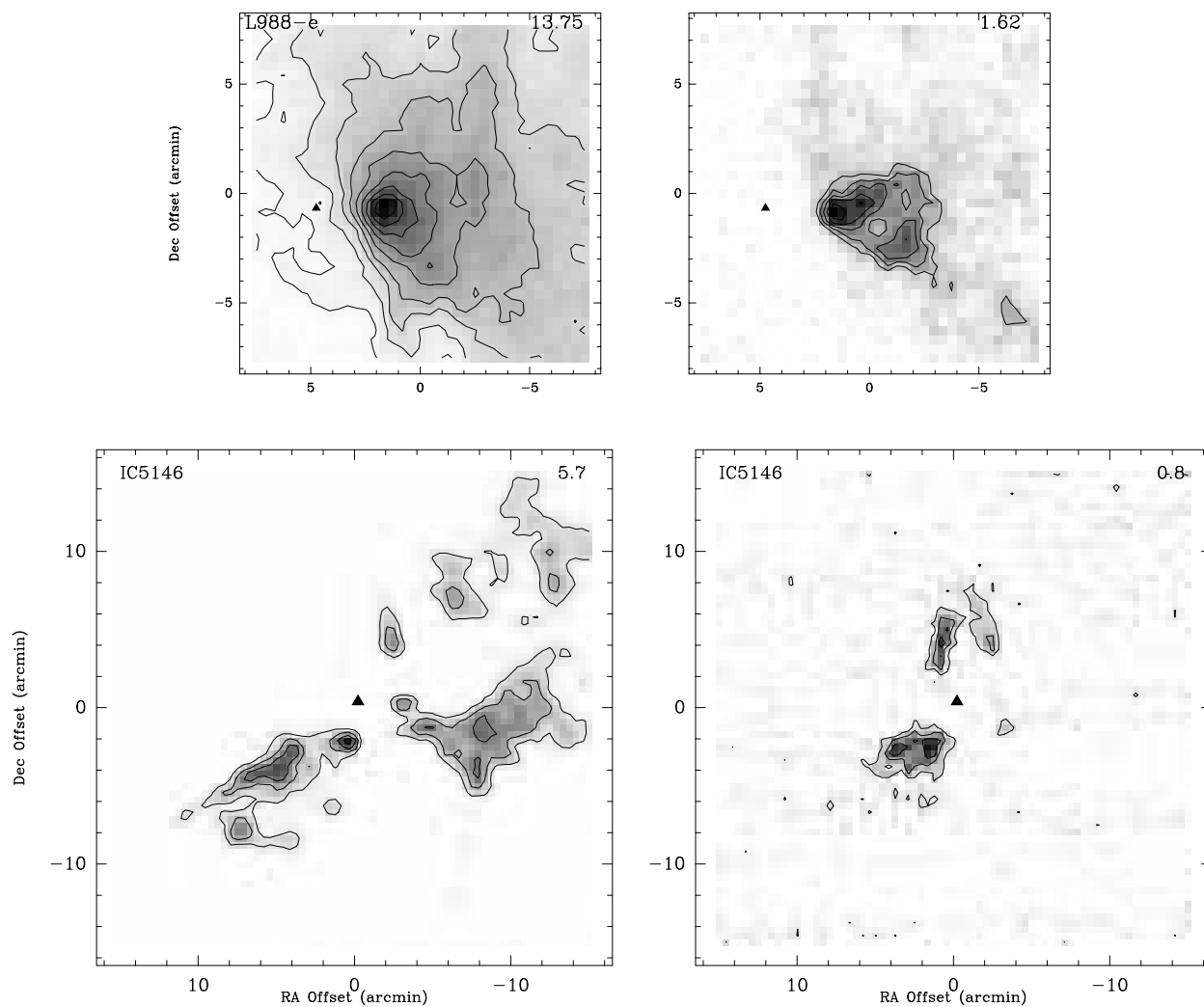


Fig. 11.— Integrated intensity maps of Class III sources L988-e (top) and IC 5146 (bottom). The value of the maximum integrated intensity in K km s^{-1} is given in the top right corner of each panel. Left panels show ^{13}CO 1–0 integrated emission, with contours at 10% intervals from 10% to 100% of the maximum integrated intensity. Right panels show integrated C^{18}O 1–0 emission. Base contour is 3σ (1σ for IC 5146), contour interval is 1σ . (0,0) positions are as given in table 1. Symbols as in figure 2.

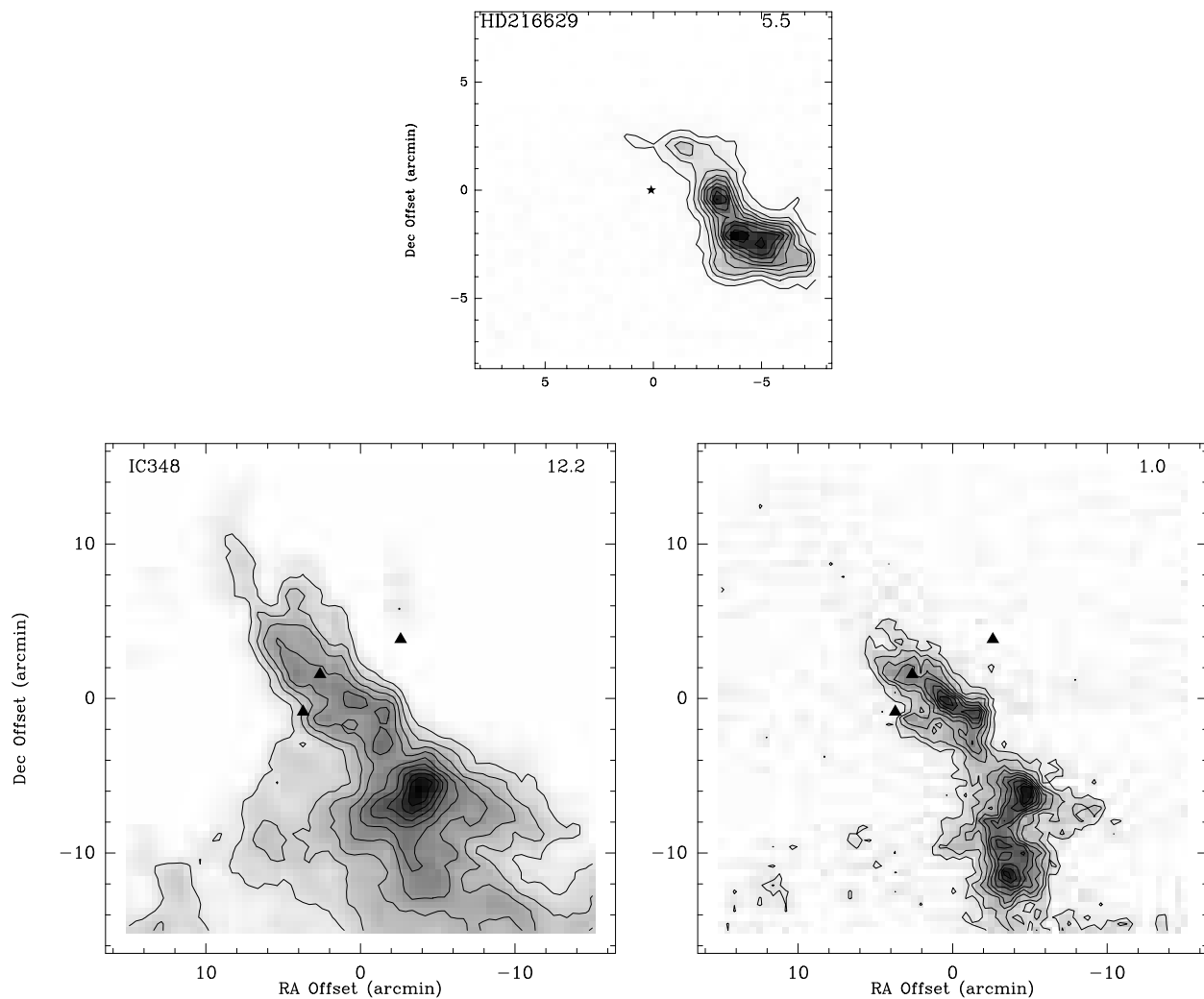


Fig. 12.— Integrated intensity maps of Class III sources HC 216629 (top) and IC 348 (bottom). The value of the maximum integrated intensity in K km s^{-1} is given in the top right corner of each panel. Left panels show ^{13}CO 1–0 integrated emission, with contours at 10% intervals from 10% to 100% of the maximum integrated intensity. Right panels show integrated C^{18}O 1–0 emission. Base contour is 3σ , contour interval is 1σ . (0,0) positions are as given in table 1. Symbols as in figure 2.

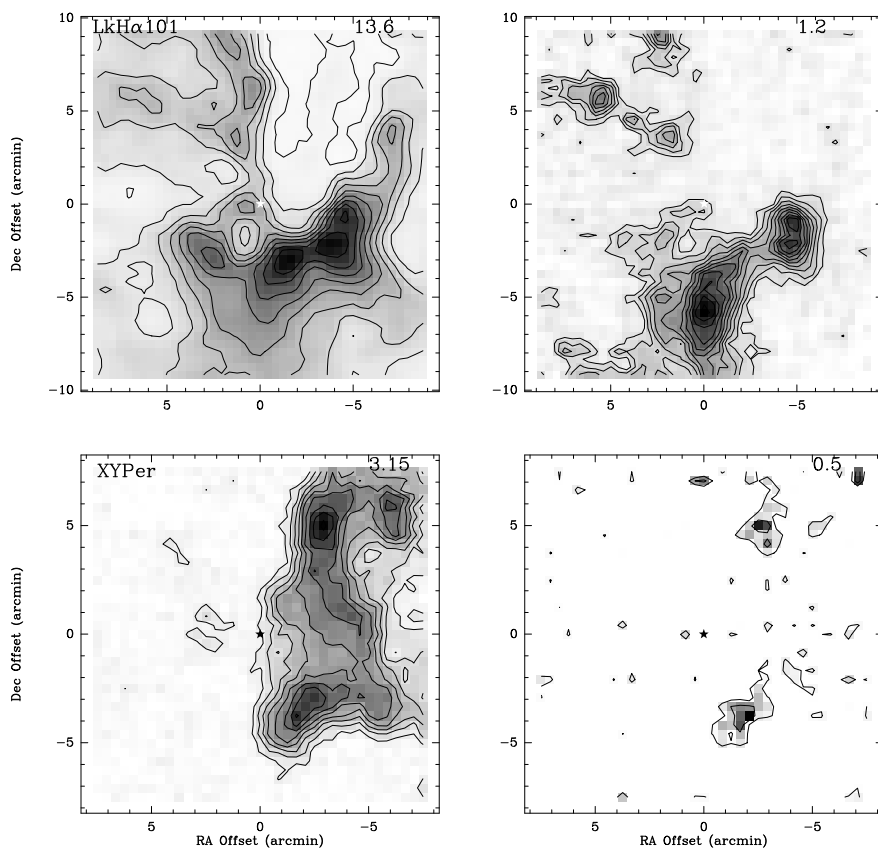


Fig. 13.— Integrated intensity maps of Class III sources LkH α 101 (top) and XY Per (bottom). The value of the maximum integrated intensity in K km s $^{-1}$ is given in the top right corner of each panel. Left panels show ^{13}CO 1–0 integrated emission, with contours at 10% intervals from 10% (3σ for XY Per) to 100% of the maximum integrated intensity. Right panels show integrated C^{18}O 1–0 emission. Base contour is 3σ (1σ for XY Per), contour interval is 1σ . (0,0) positions are as given in table 1. Symbols as in figure 2.

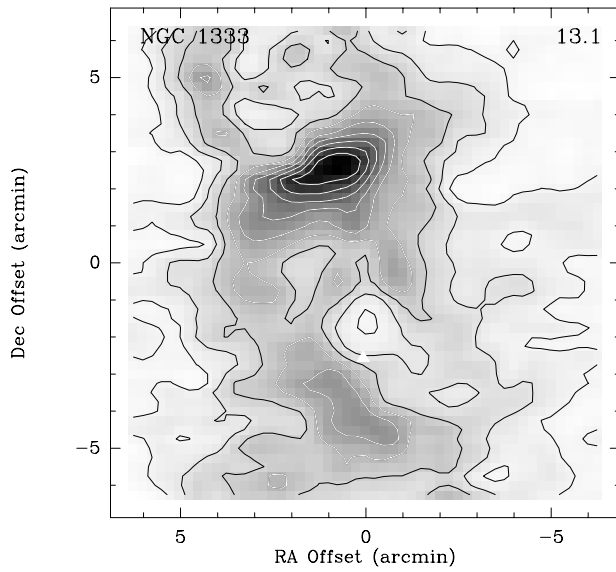


Fig. 14.— C¹⁸O 2–1 integrated intensity map of NGC 1333. Base contour is at 10%, contour interval is 10% of the maximum integrated intensity, as given in the top right corner of the panel. (0,0) positions are as given in table 1. Symbols are as in figure 2.

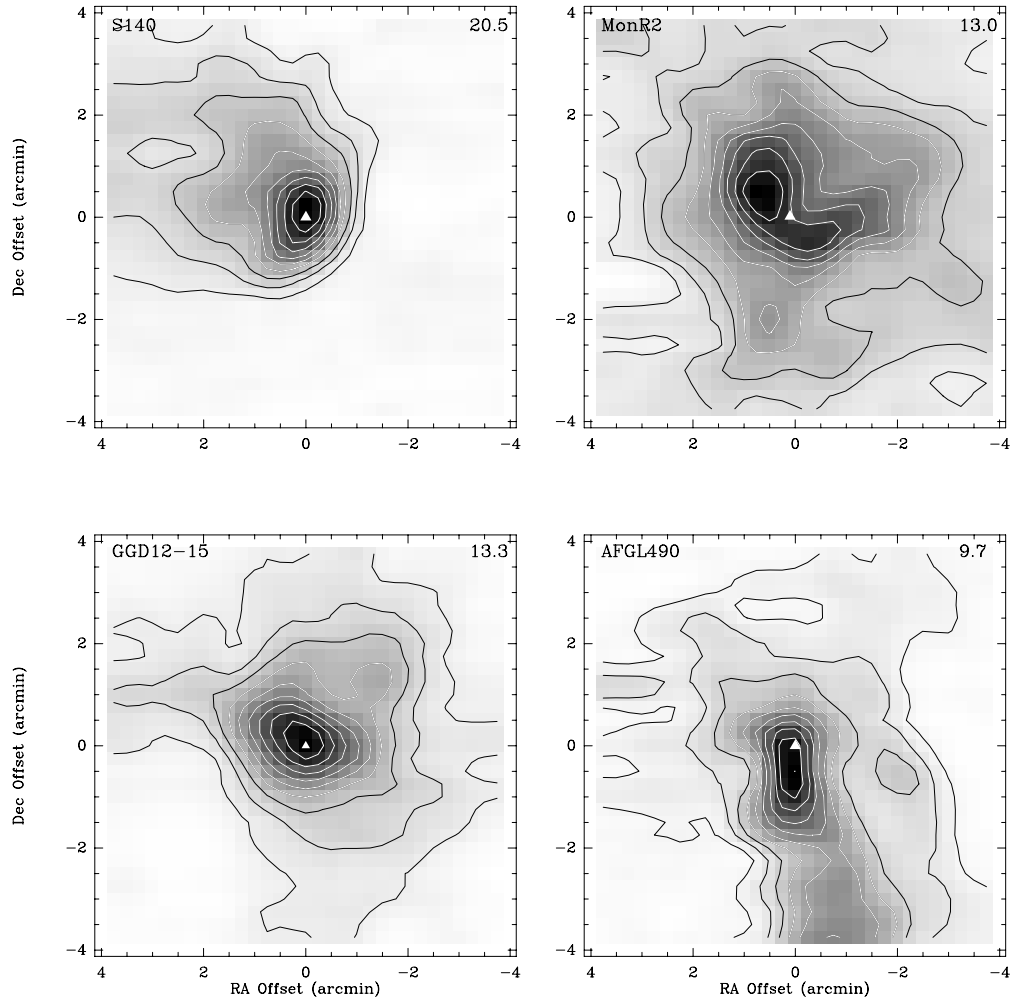


Fig. 15.— $C^{18}O$ 2–1 integrated intensity maps of S140, Mon R2, GGD 12-15 and AFGL 490. Base contour is at 10%, contour interval is 10% of the maximum integrated intensity, as given in the top right corner of each panel. (0,0) positions are as given in table 1. Symbols are as in figures 2.

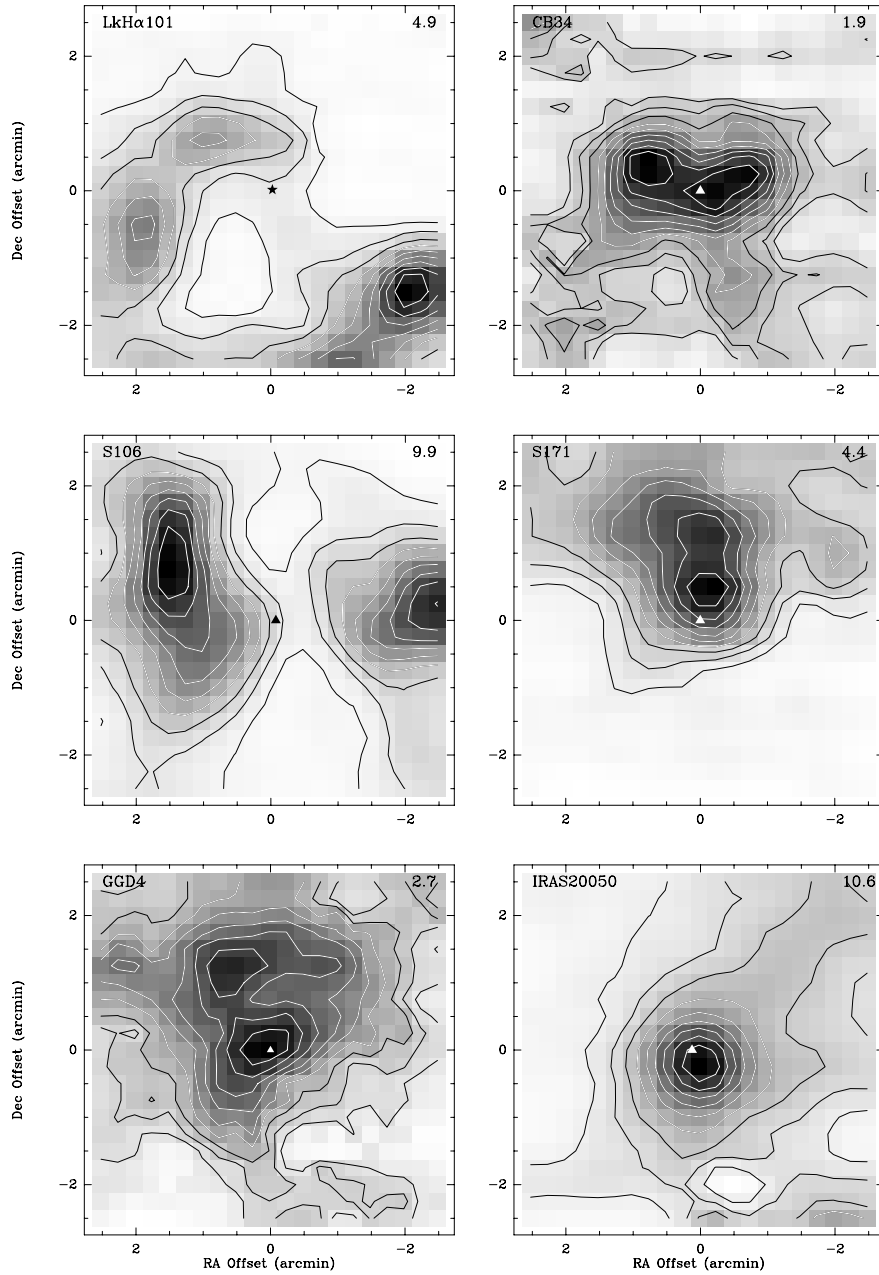


Fig. 16.— C¹⁸O 2–1 integrated intensity maps of LkH α 101, CB34, S106, S171, GGD4, and IRAS 20050. Base contour is at 10%, contour interval is 10% of the maximum integrated intensity, as given in the top right corner of each panel. (0,0) positions are as given in table 1. Symbols are as in figures 2.

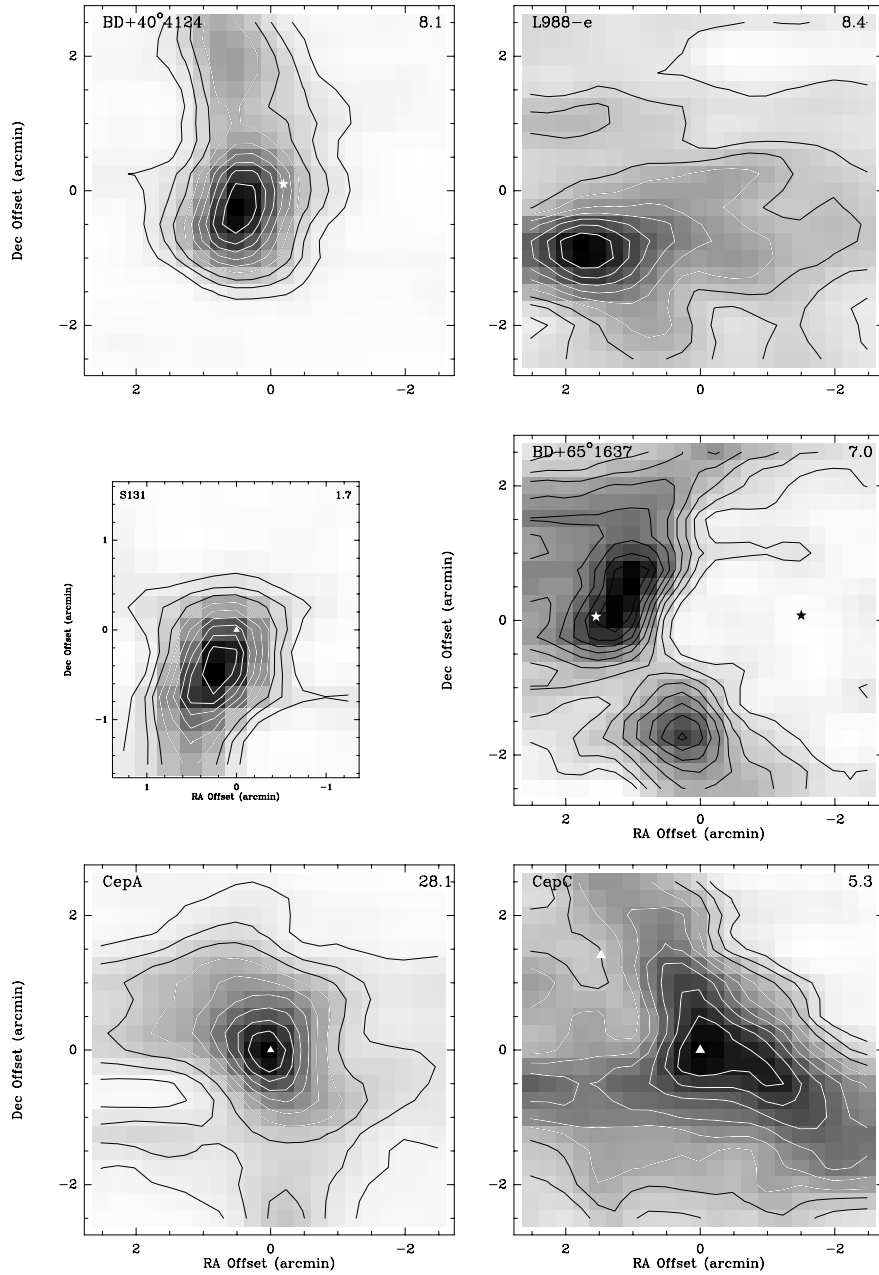


Fig. 17.— $C^{18}O$ 2–1 integrated intensity maps of BD+40°4124, L988-e, S131, NGC 7129, Cep A and Cep C. Base contour is at 10%, contour interval is 10% of the maximum integrated intensity, as given in the top right corner of each panel. (0,0) positions are as given in table 1. Symbols are as in figures 2.

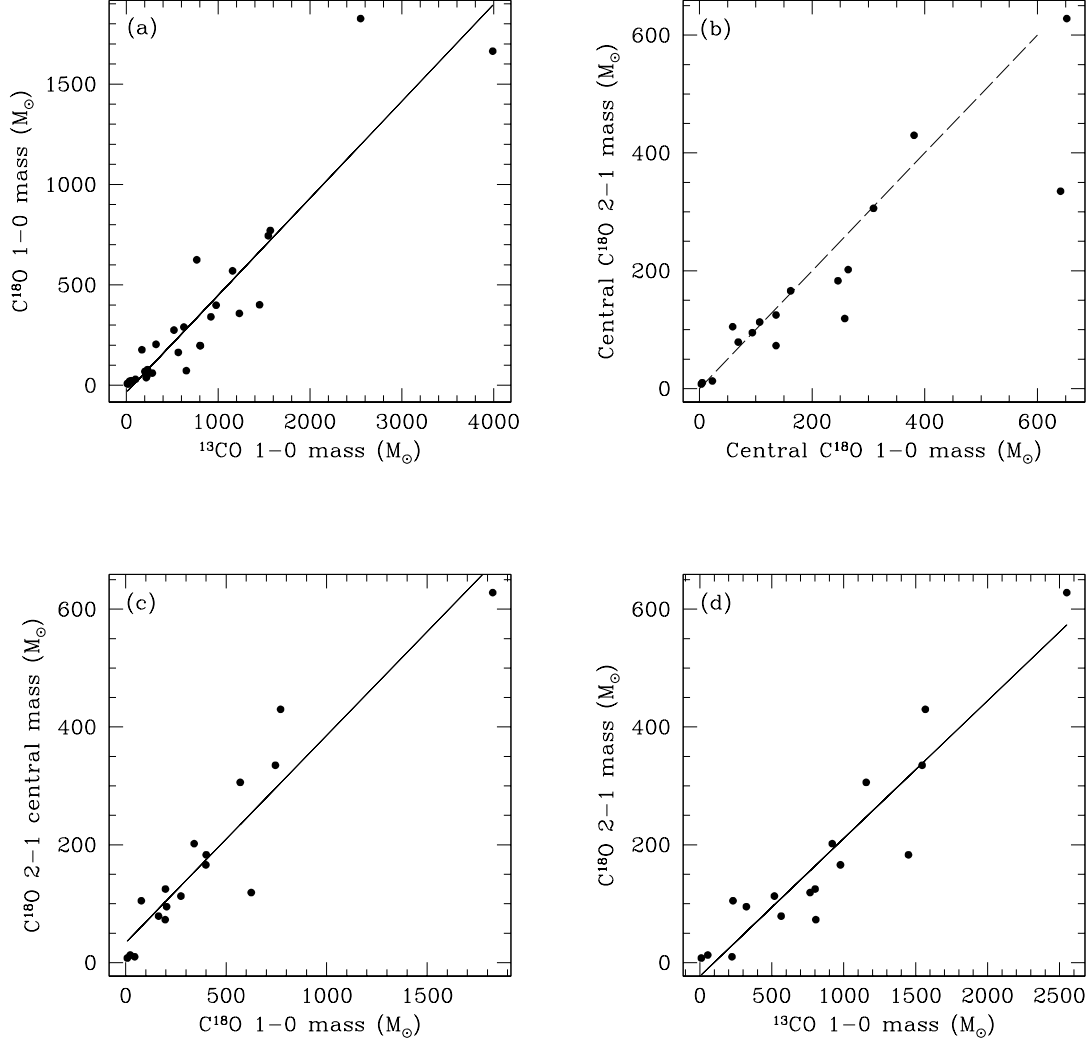


Fig. 18.— (a) C¹⁸O 1–0 mass vs. ¹³CO 1–0 mass. Solid line indicates the best-fit line with a slope of 0.48 ± 0.04 , indicating that the masses determined from the ¹³CO observations are approximately a factor of two larger. (b) Central C¹⁸O 2–1 mass vs. Central C¹⁸O 1–0 mass. The dashed line indicates a 1:1 relationship. The two most discrepant sources, GGD 12-15 and CepC are marked. (c) Central C¹⁸O 2–1 mass vs. C¹⁸O 1–0 mass. The solid line indicates a best-fit line, with a slope of 0.35 ± 0.03 . (d) Central mass from C¹⁸O 2–1 emission vs. 'total' mass from the extended ¹³CO 1–0 emission. The solid line indicates the best-fit line with a slope of 0.23 ± 0.02 .

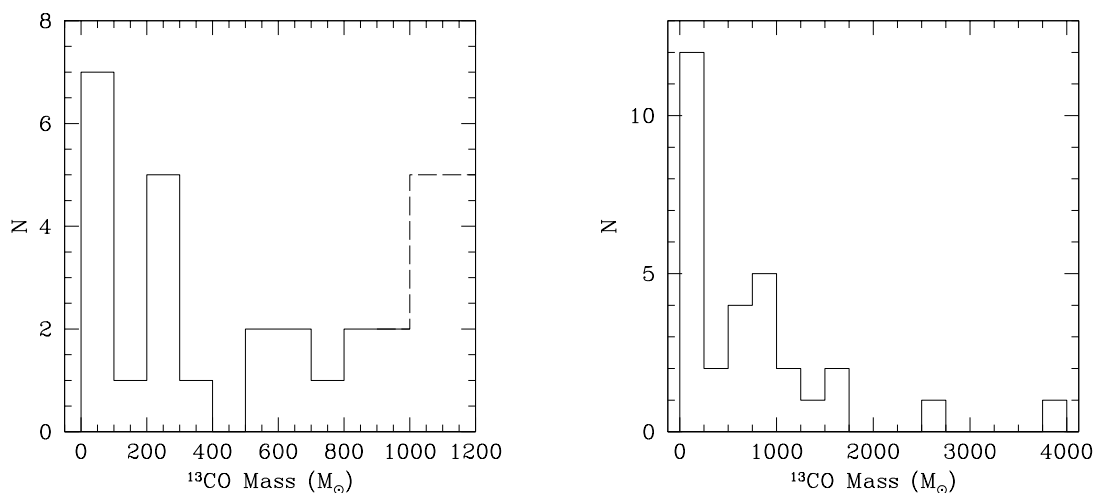


Fig. 19.— (a) Histograms of ^{13}CO 1–0 masses. Left: Expanded scale between 0 and $1000 M_{\odot}$ with bin size of $100 M_{\odot}$. Right: All sources with bin size of $250 M_{\odot}$.

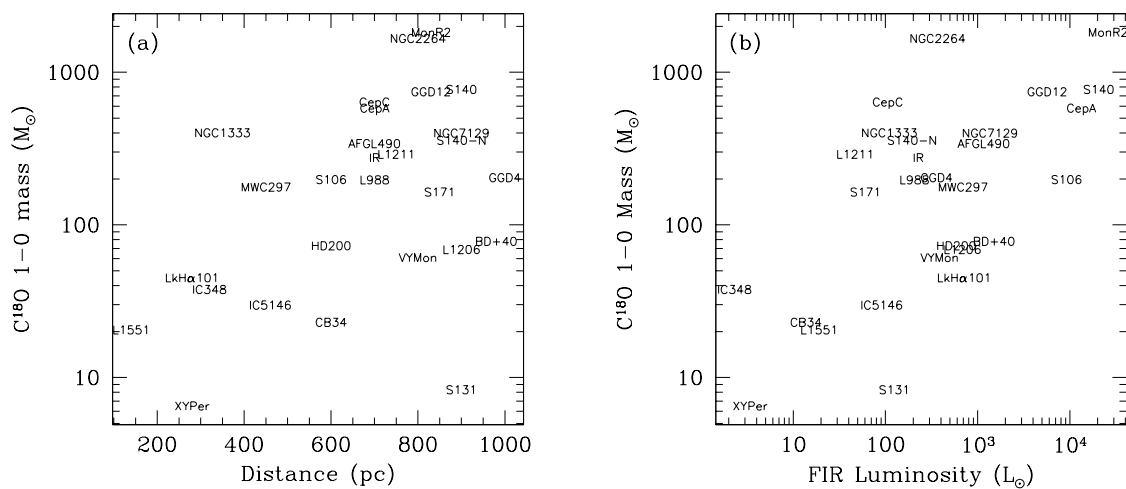


Fig. 20.— (a) C^{18}O 1–0 mass vs. distance. Some source names have been shortened for clarity: HD200 = HD 200775; IR = IRAS 20050; BD+40 = BD+40°4124; L988 = L 988-e; GGD12 = GGD 12-15. (b) C^{18}O 1–0 mass vs. FIR luminosity. Source abbreviations as for (a).

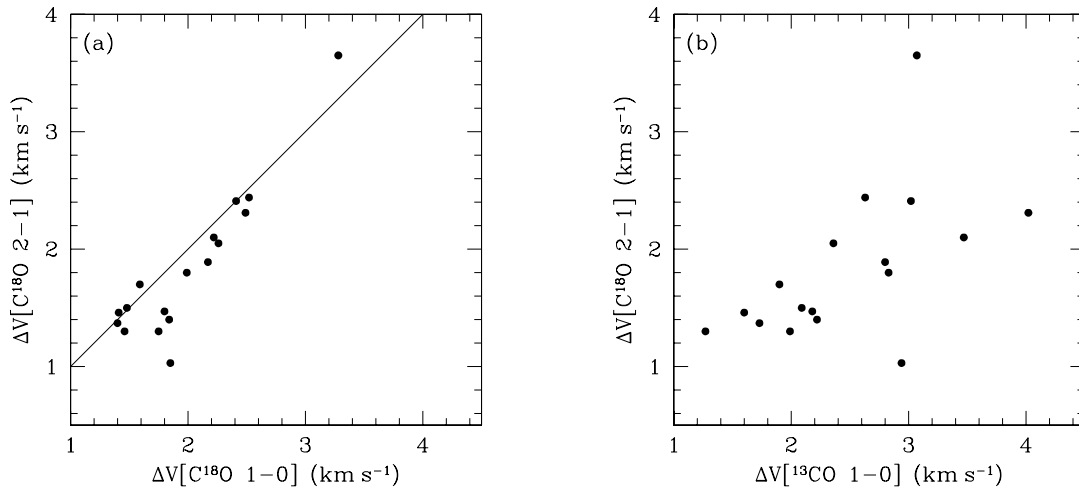


Fig. 21.— (a) Average C¹⁸O 2–1 linewidth vs. average C¹⁸O 1–0 linewidth. Solid line indicates a 1:1 relation. (b) Average C¹⁸O 2–1 linewidth vs. average ¹³CO 1–0 linewidth. The larger scatter is most likely due to optical depth effects in the ¹³CO spectra.

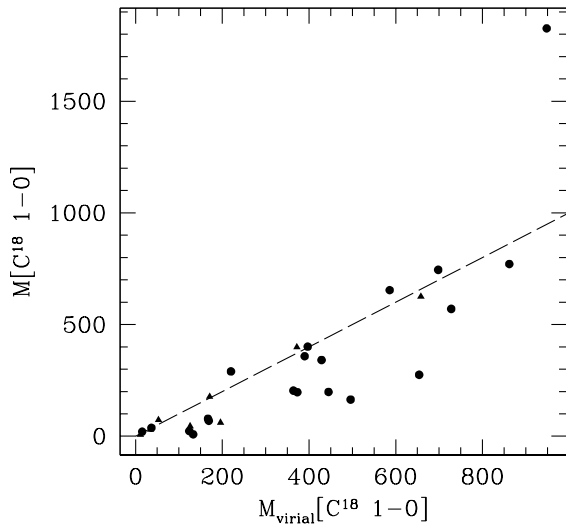


Fig. 22.— C¹⁸O 1–0 mass vs. C¹⁸O 1–0 virial mass. Circles represent sources with centrally condensed morphologies, while triangles are sources which are extended or diffuse (for which the virial mass is not really applicable). The dashed line indicates the 1:1 relation.

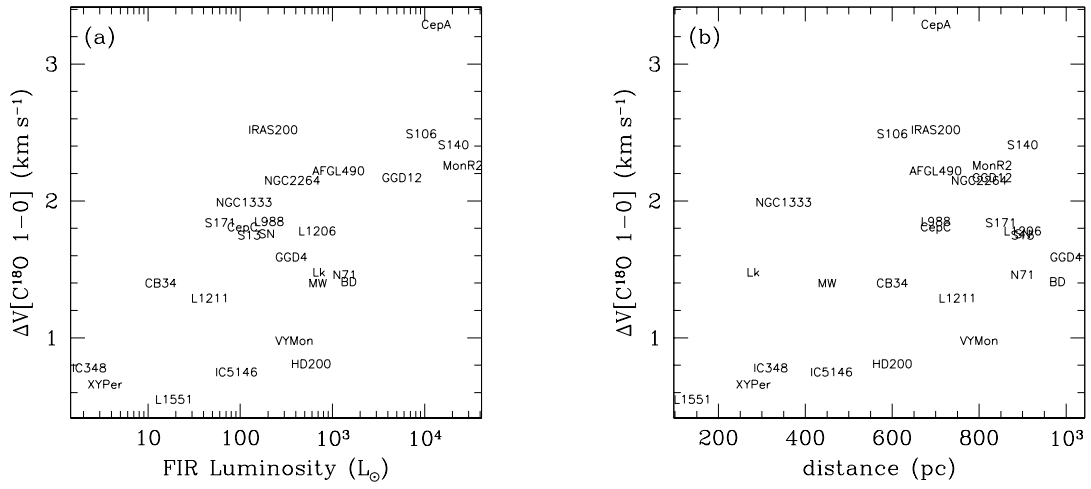


Fig. 23.— (a) Average $C^{18}O$ 1-0 linewidth vs. FIR luminosity. Some source names have been abbreviated for clarity: HD200 = HD 200775; IRAS200 = IRAS 20050; BD = BD+40°4124; N71 = NGC7129; Lk = LkH α 101; MW = MWC 297; SN = S 140-N; S13 = S 131. (b) Average $C^{18}O$ 1-0 linewidth vs. distance.

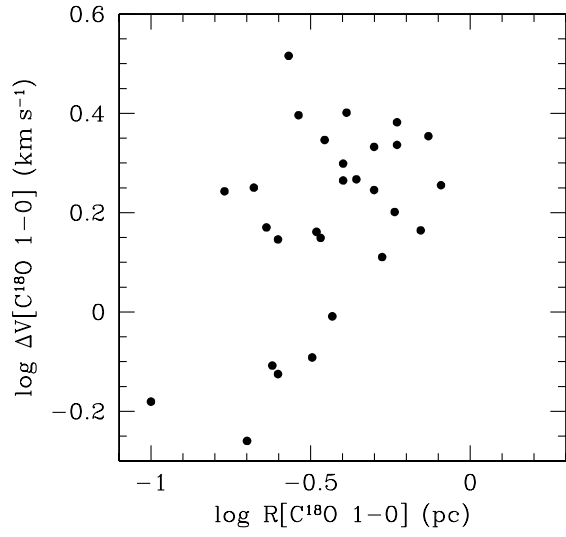


Fig. 24.— Size-linewidth relation for the $\text{C}^{18}\text{O } 1-0$ line.

Table 1. The Sample

| Source | RA(1950) hh:mm:ss | Dec(1950) dd:mm:ss | Adopted Distance pc | FIR Luminosity ^a L_{\odot} | N_{stars} | Refs. |
|-------------|----------------------|-----------------------|------------------------|--|-------------------|----------|
| MWC297 | 18:25:01.40 | −03:51:47.0 | 450 | 694.2 | 37 | 1,2 |
| VVser | 18:26:14.30 | +00:06:40.0 | 440 | 10.7 | 24 | 1,2 |
| IRAS20050 | 20:05:02.00 | +27:20:30.0 | 700 | 227.1 | ~100 | 3 |
| BD+40° 4124 | 20:18:43.32 | +41:12:11.6 | 980 | 1503 | ≥19 | 4 |
| S106 | 20:25:34.00 | +37:12:50.0 | 600 | 9205 | 160 | 5 |
| HD200775 | 21:00:59.70 | +67:57:56.0 | 600 | 585.9 | 9 | 1,2 |
| L988-e | 21:02:04.60 | +50:03:20.0 | 700 | 206.1 | 45 | 6 |
| S131 | 21:38:53.20 | +56:22:18.0 | 900 | 125.1 | ≤10 | 7,8 |
| NGC 7129 | 21:41:47.00 | +65:52:45.5 | 900 | 1360 | 29 | 1,2 |
| IC5146 | 21:51:36.23 | +47:01:54.9 | 460 | 90.8 | >100 | 17,18 |
| S140 | 22:17:41.10 | +63:03:41.6 | 900 | 20560 | ≤16 | 9 |
| S140-N | 22:17:51.10 | +63:17:50.0 | 900 | 194.1 | >10 | 9 |
| L1206 | 22:27:12.20 | +63:58:21.0 | 900 | 684.4 | 27 | 6 |
| L1211 | 22:45:23.30 | +61:46:07.0 | 750 | 47.0 | <245 ^b | 6 |
| HD216629 | 22:51:18.40 | +61:52:46.0 | 700 | 25.0 | 29 | 1,2 |
| CepA | 22:54:20.20 | +61:45:55.0 | 700 | 13320 | <580 ^b | 6 |
| CepC | 23:03:45.60 | +62:13:49.0 | 700 | 105.9 | <110 ^b | 6 |
| S171 | 00:01:23.00 | +68:17:59.0 | 850 | 60.8 | >10 | 10 |
| AFGL490 | 03:23:39.00 | +58:36:33.0 | 700 | 1167 | 45 | 6 |
| NGC1333 | 03:25:54.98 | +31:08:24.1 | 350 | 110.0 | 143 | 11 |
| IC348 | 03:41:13.14 | +32:00:52.1 | 320 | 2.3 | ~400 | 15,19,24 |
| XYPer | 03:46:17.40 | +38:49:50.0 | 280 | 3.4 | 11 | 1,2,4,12 |
| LkHα101 | 04:26:57.30 | +35:09:56.0 | 280 | 713.5 | >100 | 12,13,16 |
| L1551 | 04:28:45.14 | +18:04:44.3 | 140 | 19.1 | ≥15 | 20,21 |
| GGD4 | 05:37:21.30 | +23:49:22.0 | 1000 | 359.0 | 10 | 6 |
| CB34 | 05:44:02.40 | +20:59:22.0 | 600 | 13.8 | 12 | 14 |
| MonR2 | 06:05:20.00 | −06:22:30.0 | 830 | 26010 | 371 | 15 |
| GGD12-15 | 06:08:24.50 | −06:11:12.0 | 830 | 5682 | 134 | 15 |
| VYMon | 06:28:21.00 | +10:28:15.0 | 800 | 387.4 | 25 | 1,2 |
| NGC2264 | 06:38:10.00 | +09:40:00.0 | 800 | 367.2 | 360 | 22,23 |

Note. — Source details compiled from the literature

^aDetermined from the 12–100 μ m fluxes of the nearest IRAS point source, as described in section 2.

^bLimits indicate the estimate was not corrected for foreground or background contamination, hence the true number of stars in the cluster will be much smaller than the number quoted here.

References. — 1. Testi et al. 1998; 2. Testi, Palla, & Natta 1999; 3. Chen et al. 1997; 4. Testi et al. 1997; 5. Hodapp & Rayner 1991; 6. Hodapp 1994; 7. Sugitani et al. 1991; 8. Sugitani, Tamura, & Ogura 1995; 9. Evans et al. 1989; 10. Yang & Fukui 1992; 11. Lada, Alves, & Lada 1996; 12. A. Wilson 2002, personal communication; 13. Barsony, Schombert, & Kis-Halas 1991; 14. Alves & Yun 1995; 15. Carpenter 2000; 16. Aspin & Barsony 1994; 17. Lada, Alves, & Lada 1999; 18. Herbig & Dahm 2002; 19. Carpenter 2002; 20. Fridlund, Hultgren, & Liseau 1997; 21. Carkner et al. 1996; 22. Lada, Young, & Greene 1993; 23. Schreyer et al. 1997; 24. Lada & Lada 1995.

Table 2. Summary of Observations

| Source | FCRAO Observations | | | | SMTO Observations | | | |
|------------|----------------------|------------------------------|---------------------------|---|----------------------|------------------------------|-------------------------|-----------------------|
| | Map Size (arcmin) | Spectral Resolution (kHz) | RMS ^{a,b} (K) | Lines Observed | Map Size (arcmin) | Spectral Resolution (kHz) | RMS ^a (K) | Lines Observed |
| MWC297 | 15×15 | 25 | 0.22 | ¹³ CO 1–0, C ¹⁸ O 1–0 | ... | ... | ... | ... |
| VVSer | 15×15 | 25 | 0.25 | ¹³ CO 1–0, C ¹⁸ O 1–0 | ... | ... | ... | ... |
| IRAS20050 | 15×15 | 25 | 0.21 | ¹³ CO 1–0, C ¹⁸ O 1–0 | 5×5 | 250 | 0.20 | C ¹⁸ O 2–1 |
| BD+40°4124 | 15×15 | 50 | 0.12 | ¹³ CO 1–0, C ¹⁸ O 1–0 | 5×5 | 250 | 0.14 | C ¹⁸ O 2–1 |
| S106 | 15×15 | 25 | 0.16 | ¹³ CO 1–0, C ¹⁸ O 1–0 | 5×5 | 250 | 0.13 | C ¹⁸ O 2–1 |
| HD200775 | 15×15 | 25 | 0.22 | ¹³ CO 1–0, C ¹⁸ O 1–0 | ... | ... | ... | ... |
| L988-e | 16×16 | 25 | 0.34 | ¹³ CO 1–0, C ¹⁸ O 1–0 | 5×5 | 250 | 0.16 | C ¹⁸ O 2–1 |
| S131 | 8×8 | 25 | 0.24 | ¹³ CO 1–0, C ¹⁸ O 1–0 | 3×3 | 250 | 0.11 | C ¹⁸ O 2–1 |
| NGC7129 | 15×15 | 25 | 0.17 | ¹³ CO 1–0, C ¹⁸ O 1–0 | 5×5 | 250 | 0.17 | C ¹⁸ O 2–1 |
| IC5146 | 30×30 | 25 | | ¹³ CO 1–0, C ¹⁸ O 1–0 | ... | ... | ... | ... |
| S140 | 19×18 | 25 | 0.20 | ¹³ CO 1–0, C ¹⁸ O 1–0 | 7.5×7.5 | 250 | 0.19 | C ¹⁸ O 2–1 |
| S140-N | 15×15 | 25 | | ¹³ CO 1–0, C ¹⁸ O 1–0 | ... | ... | ... | ... |
| L1206 | 15×15 | 50 | 0.22 | ¹³ CO 1–0, C ¹⁸ O 1–0 | ... | ... | ... | ... |
| L1211 | 19×18 | 25 | 0.22 | ¹³ CO 1–0, C ¹⁸ O 1–0 | ... | ... | ... | ... |
| HD216629 | 16×16 | 25 | 0.35 | ¹³ CO 1–0, C ¹⁸ O 1–0 | ... | ... | ... | ... |
| CepA | 15×15 | 25 | 0.22 | ¹³ CO 1–0, C ¹⁸ O 1–0 | 5×5 | 250 | 0.17 | C ¹⁸ O 2–1 |
| CepC | 16×16 | 25 | 0.17 | ¹³ CO 1–0, C ¹⁸ O 1–0 | 5×5 | 250 | 0.17 | C ¹⁸ O 2–1 |
| S171 | 18×28 | 25 | 0.19 | ¹³ CO 1–0, C ¹⁸ O 1–0 | 5×5 | 250 | 0.11 | C ¹⁸ O 2–1 |
| AFGL490 | 15×15 | 50 | 0.18 | ¹³ CO 1–0, C ¹⁸ O 1–0 | 7.5×7.5 | 250 | 0.09 | C ¹⁸ O 2–1 |
| NGC1333 | 33×39 | 50 | 0.14 | ¹³ CO 1–0, C ¹⁸ O 1–0 | 12.5×12.5 | 250 | 0.17 | C ¹⁸ O 2–1 |
| IC348 | 30×30 | 25 | | ¹³ CO 1–0, C ¹⁸ O 1–0 | ... | ... | ... | ... |
| XYPe | 15×15 | 50 | 0.28 | ¹³ CO 1–0, C ¹⁸ O 1–0 | ... | ... | ... | ... |
| LkHα101 | 15×19 | 25 | 0.17 | ¹³ CO 1–0, C ¹⁸ O 1–0 | 5×5 | 250 | 0.13 | C ¹⁸ O 2–1 |
| L1551 | 30×30 | 25 | | ¹³ CO 1–0, C ¹⁸ O 1–0 | ... | ... | ... | ... |
| GGD4 | 15×15 | 25 | 0.20 | ¹³ CO 1–0, C ¹⁸ O 1–0 | 5×5 | 250 | 0.16 | C ¹⁸ O 2–1 |
| CB34 | 16×16 | 25 | 0.18 | ¹³ CO 1–0, C ¹⁸ O 1–0 | 5×5 | 250 | 0.17 | C ¹⁸ O 2–1 |
| MonR2 | 15×15 | 25 | 0.25 | ¹³ CO 1–0, C ¹⁸ O 1–0 | 7.5×7.5 | 250 | 0.11 | C ¹⁸ O 2–1 |
| GGD12-15 | 15×15 | 25 | 0.19 | ¹³ CO 1–0, C ¹⁸ O 1–0 | 7.5×7.5 | 250 | 0.14 | C ¹⁸ O 2–1 |
| VYMon | 15×15 | 50 | 0.22 | ¹³ CO 1–0, C ¹⁸ O 1–0 | ... | ... | ... | ... |
| NGC2264 | 60×60 | 25 | | ¹³ CO 1–0, C ¹⁸ O 1–0 | ... | ... | ... | ... |

^aAverage rms per channel.

^bThe noise in the ¹³CO and C¹⁸O 1–0 data is the same, as they were taken simultaneously through the same receiver. The slight difference in system temperature between the two frequencies is negligible, as is any difference in spectrometer noise.

Table 3. Morphological Properties

| Source | Morphology | N_{peaks} | d_* ^a (pc) | Developmental Type |
|------------------|------------------------|-------------|----------------------------|-----------------------|
| MWC297 | diffuse, extended | 3 | 0.25 ^b | III |
| VVser | diffuse, extended | 5 | 0.25 ^b | III |
| IRAS20050 | core + envelope | 2 | 0 | II |
| BD+40°4124 | compact core | 1 | 0 | I _{BRG} |
| S106 | compact core | 2 | 0 | II |
| HD200775 | cavity | 5 | 0.45 ^b | III |
| L988-e | core + envelope | 1 | 0.50 | III |
| S131 | compact core | 1 | 0 | I _{BRG} |
| NGC 7129 | core + cavity | 1 | 0 | II |
| IC5146 | extended | 7 | 0.12 | III |
| S140 | compact core, cometary | 1 | 0 | I _{BRG} |
| S140-N | core + envelope | 2 | 0.2 | II |
| L1206 | compact core | 1 | 0 | I _{BRG} |
| L1211 | core + envelope | 3 | 0 | II |
| HD216629 | compact core | 3 | 0.60 | III |
| CepA | compact core | 1 | 0 | I |
| CepC | extended ridge | 2 | 0.30 | II |
| S171 | compact core | 2 | 0.60 ^c | II |
| AFGL490 | core + envelope | 1 | 0 | I |
| NGC1333 | core + envelope | 1 | 0.6 | II |
| IC348 | core + ridge | 1 | 0.75 | III |
| XYPper | extended ridge | 2 | 0.25 | III |
| LkH α 101 | cavity | 2 | 0.25 ^b | III |
| L1551 | extended | 2 | 0.06 | II |
| GGD4 | compact core | 1 | 0 | I |
| CB34 | compact core | 1 | 0 | I _{BRG} |
| MonR2 | core + envelope | 1 | 0 | I |
| GGD12-15 | core + envelope | 1 | 0 | I |
| VYMon | extended ridge | 3 | 0 | II |
| NGC2264 | core + envelope | 1 | 0 | I |

^aA zero in this column indicates the position of the IRAS source or star is within 2 map pixels ($50'' \simeq 1$ beamwidth) of the position of peak ^{13}CO emission.

^bIRAS source or star is located in or close to a cavity.

^cAlthough the IRAS source *is* close to peak of C^{18}O emission.

Table 4. Masses

| (1) Source | (2) $M[^{13}\text{CO } 1-0]$ M_{\odot} | (3) $M_{\text{virial}}[^{13}\text{CO } 1-0]$ M_{\odot} | (4) $M[^{18}\text{O } 1-0]$ M_{\odot} | (5) $M_{\text{virial}}[^{18}\text{O } 1-0]$ M_{\odot} | (6) $M_{\text{central}}[^{18}\text{O } 1-0]$ M_{\odot} | (7) $M[^{18}\text{O } 2-1]$ M_{\odot} | (8) $M_{\text{virial}}[^{18}\text{O } 2-1]$ M_{\odot} |
|------------------|--|--|---|---|--|---|---|
| MWC297 | 169 | 613 | 177 | 171 | ... | ... | ... |
| VVSer | 72 | 1374 | 18 | ... | ... | ... | ... |
| IRAS20050 | 518 | 1057 | 275 | 654 | 107 | 113 | 238 |
| BD+40°4124 | 230 | 264 | 78 | 167 | 59 | 105 | 123 |
| S106 | 801 | 1919 | 198 | 445 | 136 | 125 | 320 |
| HD200775 | 653 | 341 | 73 | 53 | ... | ... | ... |
| L988-e | 806 | 1224 | 197 | 373 | 136 | 73 | 48 |
| S131 | 10 | 78 | 8.3 | 133 | 3.4 | 7.8 | 67 |
| NGC 7129 | 977 | 979 | 399 | 372 | 162 | 166 | 152 |
| IC5146 | 99.3 | 110 | 29.8 | 34.5 | ... | ... | ... |
| S140 | 1567 | 1293 | 771 | 862 | 381 | 430 | 363 |
| S140-N | 1230 | 721 | 358 | 390 | ... | ... | ... |
| L1206 | 202 | 298 | 69 | 169 | ... | ... | ... |
| L1211 | 626 | 514 | 290 | 220 | ... | ... | ... |
| HD216629 | 47 | 212 | ... | ... | ... | ... | ... |
| CepA | 1156 | 844 | 570 | 728 | 309 | 306 | 632 |
| CepC | 766 | 1204 | 625 | 658 | 258 | 119 | 189 |
| S171 | 565 | 874 | 164 | 496 | 69 | 79 | 147 |
| AFGL490 | 920 | 1655 | 341 | 429 | 264 | 202 | 308 |
| NGC1333 | 1450 | 1397 | 401 | 397 | 246 | 183 | 162 |
| IC348 | 216 | 113 | 37.7 | 36.6 | ... | ... | ... |
| pXYPer | 17 | 335 | 6.5 | 11 | ... | ... | ... |
| LkH α 101 | 223 | 361 | 45 | 126 | 5 | 10 | 50 |
| L1551 | 34.2 | 47 | 20.5 | 15.3 | ... | ... | ... |
| GGD4 | 323 | 598 | 204 | 364 | 94 | 95 | 311 |
| CB34 | 55 | 204 | 23 | 124 | 23 | 13 | 85 |
| MonR2 | 2550 | 911 | 1826 | 948 | 652 | 628 | 462 |
| GGD12-15 | 1545 | 1234 | 745 | 698 | 641 | 335 | 241 |
| VYMon | 282 | 432 | 61 | 196 | ... | ... | ... |
| NGC2264 | 3988 | 1517 | 1664 | 586 | ... | ... | ... |

Table 5. Linewidths and Sizes

| (1) Source | (2) $\Delta V[^{13}\text{CO } 1-0]$ km s^{-1} | (3) $R[^{13}\text{CO } 1-0]$ pc | (4) $\Delta V[\text{C}^{18}\text{O } 1-0]$ km s^{-1} | (5) $R[\text{C}^{18}\text{O } 1-0]$ pc | (6) $\Delta V[\text{C}^{18}\text{O } 2-1]$ km s^{-1} | (7) $R[\text{C}^{18}\text{O } 2-1]$ pc |
|------------------|--|---------------------------------------|---|--|---|--|
| MWC297 | 1.89 | 0.68 | 1.45 | 0.33 | ... | ... |
| VVser | 2.60 | 0.81 | 1.19 | ... | ... | ... |
| IRAS20050 | 2.63 | 0.61 | 2.52 | 0.41 | 2.44 | 0.16 |
| BD+40°4124 | 1.60 | 0.41 | 1.41 | 0.34 | 1.46 | 0.23 |
| S106 | 4.02 | 0.47 | 2.49 | 0.29 | 2.31 | 0.24 |
| HD200775 | 1.51 | 0.60 | 0.81 | 0.32 | ... | ... |
| L988-e | 2.94 | 0.57 | 1.85 | 0.44 | 1.03 | 0.18 |
| S131 | 1.27 | 0.19 | 1.75 | 0.17 | 1.30 | 0.16 |
| NGC 7129 | 1.99 | 0.99 | 1.46 | 0.70 | 1.30 | 0.36 |
| IC5146 | 1.1 | 0.36 | 0.75 | 0.25 | ... | ... |
| S140 | 3.02 | 0.57 | 2.41 | 0.59 | 2.41 | 0.25 |
| S140-N | 1.87 | 0.83 | 1.76 | 0.50 | ... | ... |
| L1206 | 1.70 | 0.41 | 1.78 | 0.21 | ... | ... |
| L1211 | 1.61 | 0.79 | 1.29 | 0.53 | ... | ... |
| HD216629 | 1.60 | 0.33 | ... | ... | ... | ... |
| CepA | 3.07 | 0.36 | 3.28 | 0.27 | 3.65 | 0.19 |
| CepC | 2.18 | 1.01 | 1.80 | 0.81 | 1.47 | 0.35 |
| S171 | 2.22 | 0.71 | 1.84 | 0.40 | 1.40 | 0.30 |
| AFGL490 | 3.47 | 0.55 | 2.22 | 0.35 | 2.10 | 0.28 |
| NGC1333 | 2.83 | 0.69 | 1.99 | 0.40 | 1.80 | 0.20 |
| IC348 | 1.3 | 0.27 | 0.78 | 0.24 | ... | ... |
| XYPper | 2.16 | 0.29 | 0.66 | 0.10 | ... | ... |
| LkH α 101 | 2.09 | 0.33 | 1.48 | 0.23 | 1.50 | 0.09 |
| L1551 | 0.79 | 0.30 | 0.55 | 0.20 | ... | ... |
| GGD4 | 1.90 | 0.66 | 1.59 | 0.58 | 1.70 | 0.43 |
| CB34 | 1.73 | 0.27 | 1.40 | 0.25 | 1.37 | 0.18 |
| MonR2 | 2.36 | 0.65 | 2.26 | 0.74 | 2.05 | 0.44 |
| GGD12-15 | 2.80 | 0.63 | 2.17 | 0.59 | 1.89 | 0.27 |
| VYMon | 1.46 | 0.81 | 0.98 | 0.37 | ... | ... |
| NGC2264 | 2.72 | 0.82 | 2.15 | 0.50 | ... | ... |